Submitted to ApJ
Preprint typeset using LaTeX style emulateapj v. 04/03/99

arXiv:astro-ph/9904130v1 11 Apr 1999

THE PROPERTIES OF THE GALACTIC BAR IMPLIED BY GAS KINEMATICS IN THE INNER MILKY WAY

Benjamin J. Weiner[1,2] and J. A. Sellwood[2]
[1]Observatories of the Carnegie Institution of Washington,
813 Santa Barbara St, Pasadena, CA 91101
[2]Department of Physics and Astronomy, Rutgers, The State University
136 Frelinghuysen Road, Piscataway, NJ 08854-8019
Electronic mail: bjw@ociw.edu, sellwood@physics.rutgers.edu

Rutgers Astrophysics Preprint No. 236
Submitted to ApJ

ABSTRACT

Longitude-velocity ($\ell - V$) diagrams of H I and CO gas in the inner Milky Way have long been known to be inconsistent with circular motion in an axisymmetric potential. Several lines of evidence suggest that the Galaxy is barred, and gas flow in a barred potential could be consistent with the observed "forbidden" velocities and other features in the data. We compare the H I observations to $\ell - V$ diagrams synthesized from 2–D fluid dynamical simulations of gas flows in a family of barred potentials. The gas flow pattern is very sensitive to the parameters of the assumed potential, which allows us to discriminate among models. We present a model that reproduces the outer contour of the H I $\ell - V$ diagram reasonably well; this model has a strong bar with a semimajor axis of 3.6 kpc, an axis ratio of approximately 3:1, an inner Lindblad resonance (ILR), and a pattern speed of 42 km s^{-1} kpc^{-1}, and matches the data best when viewed from 34° to the bar major axis. The behavior of the models, combined with the constraint that the shocks in the Milky Way bar should resemble those in external barred galaxies, leads us to conclude that wide ranges of parameter space are incompatible with the observations. In particular we suggest that the bar must be fairly strong, must have an ILR, and cannot be too end-on, with the bar major axis at $35° \pm 5°$ to the line of sight. The H I data exhibit larger forbidden velocities over a wider longitude range than are seen in molecular gas; this important difference is the reason our favored model differs so significantly from other recently proposed models.

Subject headings: Galaxies: Kinematics and Dynamics — Galaxies: The Galaxy — Galaxy: Kinematics and Dynamics — Galaxy: Structure — ISM: Kinematics and Dynamics — Radio lines: ISM

1. INTRODUCTION

The structure and morphology of the inner Milky Way are difficult to determine due both to dust obscuration and to our edge-on view. The canonical picture of the Milky Way as an axisymmetric spiral galaxy was enshrined in the models of Schmidt (1965), Bahcall & Soneira (1980), Ostriker & Caldwell (1983), Kent (1992), and others. However, the suggestion by de Vaucouleurs (1964) that the Galaxy is barred has been supported by many recent studies (cf. the reviews of Blitz *et al.* 1993 and Kuijken 1996). What was once thought of as the bulge now seems to be, at least in part, a thickened bar. Lines of evidence for a bar include: the infrared surface brightness distribution (Blitz & Spergel 1991; Dwek *et al.* 1995), the distribution of Mira variables (Whitelock & Catchpole 1992), IRAS point sources (Weinberg 1992, Nikolaev & Weinberg 1997), the magnitude offset of bulge stars at positive and negative longitudes (Stanek 1995; Stanek *et al.* 1997), OH/IR stars (Sevenster 1995), and the gas motions near the Galactic center (*e.g.* Liszt & Burton 1980; Binney *et al.* 1991). Several groups have used infrared photometry, especially from the COBE/DIRBE data, to deduce the density distribution in the Galactic bar (*e.g.* Blitz & Spergel 1991; Dwek *et al.* 1995; Binney, Gerhard & Spergel 1997).

It has long been known, from both 21 cm and mm observations of gaseous emission lines, that the kinematics of gas toward the Galactic center ($|l| \lesssim 10°$) are inconsistent with purely circular motions (*e.g.* Rougoor & Oort 1960, Kerr & Westerhout 1965, Oort 1977). Figure 1 shows the H I longitude–velocity ($\ell - V$) diagram constructed from the data of Liszt & Burton (1980; see also Burton & Liszt 1983). This diagram shows the distribution of H I radial velocities at galactic longitudes $13° > \ell > -11°$. Most gas is approaching at negative longitudes and receding at positive, which is the general sense of rotation of the Milky Way, but there is significant emission from gas moving in the opposite sense on both sides; such gas is inconsistent with simple circular orbits and is said to have "forbidden velocities." Forbidden velocities in excess of 100 km s^{-1} are observed throughout the range $-6° < \ell < 6°$.

A variety of explanations for the non-circular motions have been proposed including explosive outflows (cf. Oort 1977), spiral density waves (*e.g.* Scoville, Solomon & Jefferts 1974), and barlike perturbations. If the non-circular motions do result from gas flow in a non-axisymmetric potential, observation and detailed modeling of the gas kinematics should provide strong constraints on the mass distribution in the inner Galaxy. In fact, flow patterns in barred galaxy models have already been shown to provide qualitative fits to the observations (*e.g.* Peters 1975; Liszt & Burton 1980; van Albada 1985b; Mulder & Liem 1986;

Binney *et al.* 1991).

Features in diagrams such as Figure 1 contain information about the distribution of gas in space and velocity within the disk of the Galaxy. But because we cannot determine the distance to individual parcels of gas, there is no unique way to invert the observed $\ell - V$ diagram to determine the two-dimensional distribution of gas in the Galaxy; the projection into ℓ and V space is highly degenerate. Even if such a deprojection were available, we still could not use the flow pattern to deduce the galactic gravitational potential directly, since the gas is also subject to pressure forces and its motion is governed by the non-linear equations of fluid dynamics.

Thus the data need to be interpreted by comparison with models. Binney *et al.* (1991) compare stellar orbits in a barred model with the CO and H I $\ell - V$ diagrams, which offers some insight, but omits the effects of the strong shocks expected in gas flows in a bar. Subsequently, several numerical methods have been employed to construct improved models for the gas. Jenkins & Binney (1994) used sticky particles, Englmaier & Gerhard (1998) used smoothed particle hydrodynamics (SPH), while Fux (1997,1999) combined SPH and N-body techniques to attempt to build a fully self-consistent model of the inner Milky Way. Fux (1999) has compared the gas kinematics in such a model to "arm" features in the CO and H I $\ell - V$ diagrams to constrain the properties of the bar; his approach is complementary to ours, concentrating on high-density regions of the $\ell - V$ diagram.

Most modeling efforts have been devoted to observations of the dense molecular gas while comparatively little attention has been devoted to the H I data. Here we focus on the $\ell - V$ diagram for the H I, which is less affected by two principal limitations of the molecular data: the $\ell - V$ diagram for the H I is both more symmetric and more complete than the corresponding CO plots. In particular, CO (Dame *et al.* 1987; Bally *et al.* 1988) is not detected where H I emission is present in some significant regions of the $\ell - V$ plane; for example, between $\ell = 0°$ and $-6°$, the H I emission extends to ~ -270 km s^{-1} while the CO emission extends to ~ -220 km s^{-1} only (Figure 4 of Dame *et al.*). More importantly, H I emission extends to higher forbidden velocities over a wider angular range in comparison with that observed in CO.

We attempt to place constraints on the properties of the Galactic bar by comparing the H I $\ell - V$ diagram with similar plots synthesized from many fluid-dynamical models in various potentials. The full gas velocity field allows us to determine which regions of the Galaxy are responsible for prominent features of the $\ell - V$ diagram. Our goal is not to identify a unique model, but rather to infer properties of the inner Galaxy that appear to be required by the data. We conclude that the Galaxy must have a strong bar that rotates fairly quickly and has a central density high enough to produce an inner Lindblad resonance. The bar must have a semi-major axis $a \gtrsim 3$ kpc, and be viewed obliquely, with the bar major axis between 30° and 40° to the Sun–Galactic Center line.

2. THE GALACTIC LONGITUDE–VELOCITY DIAGRAM

2.1. *Observational data*

We use the H I observations of the inner Galaxy by Burton & Liszt (1978, 1983; and Liszt & Burton 1980), which produced the $\ell - V$ diagram shown in Figure 1. These data have uniform coverage of the longitude range $\ell = -11°$ to $+13°$, with spatial resolution $\sim 0.5°$, well matched to the resolution of our simulations, and good velocity resolution (2.75 km s^{-1}) and sensitivity. H. Liszt kindly provided the data in electronic form. The spectra are taken on an 0.5° grid in ℓ and b; because we are comparing to 2-D simulations, we summed the data along the b axis. We also smoothed in V with a Gaussian of $\sigma = 5.5$ km s^{-1}. A high-velocity H I cloud at $\ell = 8°, b = -4°$ and $V = -210$ km s^{-1} ("Shane's feature," Saraber & Shane 1974), was excluded from the dataset.

Plots of individual latitude slices (Burton & Liszt 1978; Liszt & Burton 1980) show that the velocity "peaks" in Figure 1 are prominent at latitudes near $b = 0°$. The broad band of emission (sometimes called the "main maximum") at $-100 < V < 100$ km s^{-1} at all longitudes is present over the entire latitude range observed by Liszt & Burton ($-6° < b < 6°$). Since the half-thickness of the gas layer is approximately 250 pc inside the Solar radius to 4 kpc radius, and the thickness may be only 100 kpc inside 4 kpc (Mihalas & Binney 1981; Jackson & Kellman 1974), the band of emission is presumably from disk gas that is relatively close by. The velocity extent of the band is large for the velocity dispersion of the gas as derived by Gunn, Knapp & Tremaine (1979), even given the 1000:1 density contrast. It is presumably attributable to line-of-sight integration over substantial bulk motions in the disk such as spiral arm streaming motions (Burton & Liszt 1983).

Foreground gas is also responsible for 21 cm absorption against the central continuum source at $\ell = 0°$, $b = 0°$. This absorption appears at negative velocity (Burton & Liszt 1978, 1993) and is visible in the summed data in some of the intermediate contours in Figure 1, although it is not conspicuous in the extreme contour. The absorption at negative velocities implies that the negative-velocity gas at $\ell = 0°$, $b = 0°$ is between the Sun and the Galactic Center, while the positive velocity gas at that position is behind the Center (Burton & Liszt 1978).

The filled circles in Figure 1 mark the points of the observed extreme-velocity contour (EVC) we will use for comparison to the simulations. Because we are interested in the motions of the gas in the inner Galaxy, we do not use that portion of the EVC that appears to be substantially influenced by foreground disk gas, but we retain the data point at $\ell = 0°$ since the extreme contour there is not much affected by absorption.

The $\ell - V$ diagram is not perfectly two-fold rotationally symmetric in many respects. Here we simply note that the shapes of the velocity peaks in the EVC differ: that at positive ℓ lies at 3° while the most negative velocity is at $\ell = -4°$, although the magnitudes are similar. More detailed plots of the H I $\ell - V$ diagram reveal other non-symmetric features in the interior of the diagram, including the well-known "3-kpc expanding arm" (*e.g.* Peters 1975; Burton & Liszt 1983, 1993), which is marginally visible in Figure 1 at $-3° > \ell > -9°$ near -100 km s^{-1}. Some investigators (*e.g.* Kerr 1967; Liszt & Burton 1980) have also presented evidence that the H I gas distribution in the inner Galaxy is tilted out of the Galactic plane. By summing the data over b, we have suppressed this aspect,

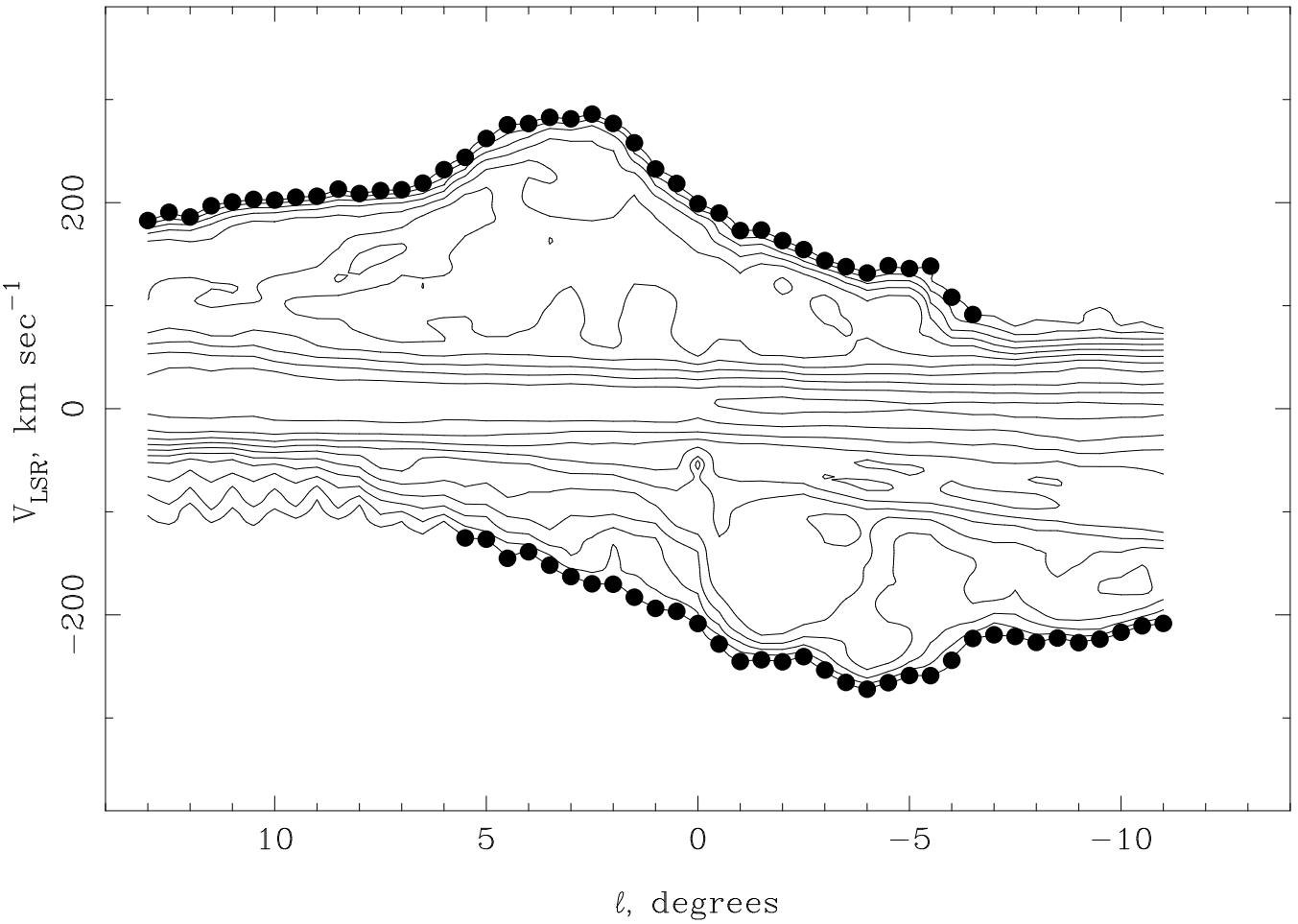

FIG. 1.— The longitude–velocity diagram of H I in the inner Galaxy from the data of Liszt & Burton (1980). The lowest contour is 0.125 K in antenna temperature summed over b, or 1.25 $M_\odot$ kpc^{-2} deg^{-1} / km s^{-1} of atomic gas (H+He), and the contours increase geometrically by a factor of 2. The forbidden quadrants are positive V at negative ℓ, and negative V at positive ℓ. The band of emission at $|V| \lesssim 100$ km s^{-1} is foreground from the disk. The filled circles are those data points on the extreme-velocity contour that we try to reproduce in the simulations.

which would be difficult to address in any case since our models are two-dimensional.

2.2. *Interpreting the extreme-velocity contour*

One must make assumptions in order to extract information on the structure of the Galaxy from the $\ell - V$ diagram. The simplest approach is to assume that the Galaxy is axisymmetric and the gas moves on circular orbits.

With this assumption (and others noted below), the $\ell - V$ diagram can be used to determine the rotation curve of the Galaxy interior to the Solar circle by the tangent-point method (cf. Gunn *et al.* 1979, Mihalas & Binney 1981). The critical feature of the $\ell - V$ diagram in this method is the extreme-velocity contour (EVC), which is the outer contour of the gas distribution in longitude–velocity space; it is the highest absolute radial velocity observed along the line of sight at each ℓ. In the tangent-point method, the EVC in the upper left and lower right quadrants only is used; gas at forbidden velocities is ignored. The extreme observed velocity needs to be corrected for instrumental resolution and the velocity dispersion of the gas, which is assumed to have a uniform value (Gunn *et al.* 1979), to find the terminal velocity at each longitude, $v_t(\ell)$ (see Section 4.1 below). With the further assumptions that some H I gas exists at every tangent point and that the circular angular frequency, $\Omega(R)$, decreases monotonically from the center, $v_t(\ell)$ yields the Galactic rotation curve $\Theta(R)$ directly through the equation $\Theta(R_0\ |\sin\ell|) = |\mathrm{v_t}(\ell)| + \Theta_0\ |\sin\ell|$.

As the correction term for the circular velocity of the LSR is small at longitudes near 0°, the EVC on the maximum side (positive V at positive ℓ, negative V at negative ℓ) is approximately the rotation curve under the axisymmetric assumption.

For circular orbits, on one side of the Galactic center all the gas should be coming towards the Sun, and on the other side it should be going away. Hence, the EVC on the non-maximum side, in the upper right and lower left quadrants of the $\ell - V$ diagram, should be featureless and close to 0 km s^{-1} (as long as the circular frequency at R_0 is less than the circular frequency in the inner Galaxy, which is true for any reasonable rotation curve). The velocity dispersion of the gas and bulk motions in the disk will push the EVC beyond 0 km s^{-1}, but apart from these effects the non-maximum EVC should not tell us much.

Figure 2 shows an $\ell - V$ diagram for a model with gas all on circular orbits. The rotation curve that gives rise to this $\ell - V$ diagram is plotted in Figure 3. The contrast with

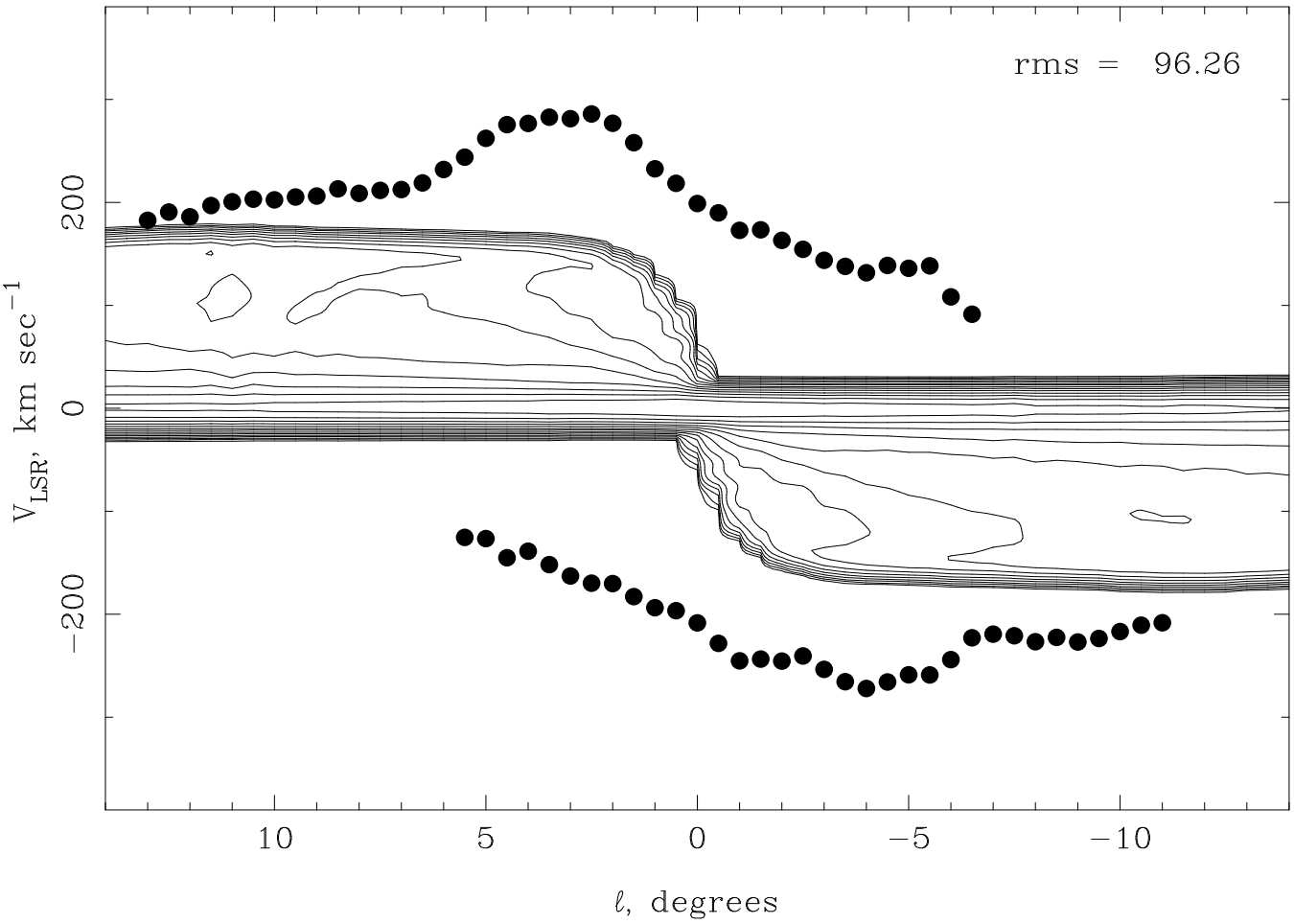

FIG. 2.— The longitude-velocity diagram of gas in an axisymmetric model. There is no gas in the forbidden quadrants, beyond the velocity dispersion-induced spread. The lowest contour is 1.7 $M_\odot$ kpc^{-2} deg^{-1} / km s^{-1} of total gas. The contours increase geometrically by a factor of 2. The filled circles are the EVC from the data in Figure 1. Simply rearranging some of the mass of this model into a bar yields a model that fits these data points quite well.

Figure 1 is instructive. Gas at forbidden velocities in the Milky Way is clearly inconsistent with a simple circular flow pattern.

The EVC is still a useful probe of the Galactic mass distribution even when the gas is *not* on circular orbits, provided that the observed tracer is ubiquitous in the disk and that the non-circular motions are caused by streaming in a non-axisymmetric potential, as first proposed by de Vaucouleurs (1964). As long as the observations are sensitive enough to pick up the tracer in regions of low density, the EVC depends almost solely on the velocity field, and variations in the fraction of gas mass in a given tracer phase are much less important. Here we discount the alternative possibility that non-circular motions arise from explosions or other violent events near the Galactic Center (cf. Oort 1977).

Neutral hydrogen is ubiquitous in the Galactic disk and is readily detectable through its 21 cm emission. It is clearly more widespread than CO in the inner Galaxy, since there are no "holes" in the H I $\ell-V$ diagram (Figure 1) in contrast with that for the CO (*e.g.* Figure 4 of Dame *et al.* 1987, and Figure 4 of Bally *et al.* 1988). Additionally, as noted earlier, the negative velocity peak of the CO $\ell - V$ diagram reaches only to -220 km s^{-1} at $\ell = -2°$ while that peak reaches -270 km s^{-1} at $\ell = -4°$ in the H I $\ell-V$ diagram, and the forbidden emission extends further in H I than in CO, especially for negative velocities at $0° < \ell < 5°$.

The interior of an $\ell - V$ diagram for CO shows much substructure with strong density contrasts, whereas that for H I exhibits only mild variations (Figure 1). Interior features, in both molecular and atomic gas, provide extra information to constrain models; *e.g.* Fux (1999) attempts to match them to an SPH gas flow in a model of the Galaxy.

The additional substructure in molecular emission, which traces gas of higher density, is probably caused by variations both in the atomic fraction and in molecular emissivity (*e.g.* temperature). Such variations, even if they are well understood, would be very hard to model, however. The EVC of the H I $\ell-V$ diagram, on the other hand, is insensitive to density variations. All successful models of the inner Milky Way should therefore match it provided only that there is *some* atomic gas everywhere in the flow. The smoothness of the EVC in Figure 1 gives us grounds to hope that this requirement is fulfilled.

3. SIMULATIONS OF THE GAS FLOW

We use a two-dimensional grid-based gas dynamical code to simulate the gas flow in models for the galactic

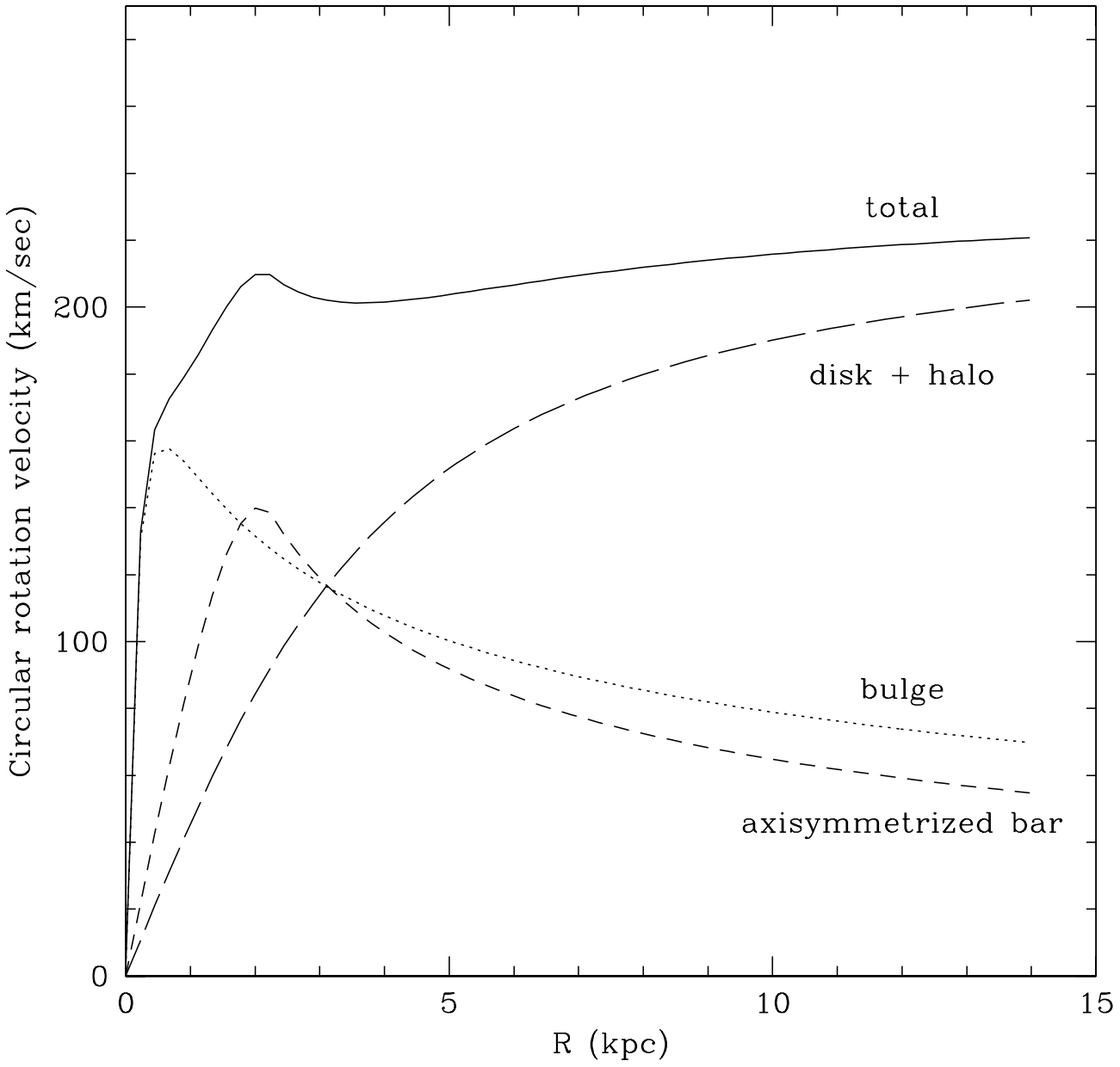

FIG. 3.— The rotation curve for the axisymmetric model. This model is the axially symmetrized mass distribution of our Model 1.

potential. The code was originally written by G. D. van Albada to model gas flow in barred galaxy potentials (van Albada 1985a, 1985b) and kindly provided by E. Athanassoula. She used it (Athanassoula 1992b) to study gas flow patterns in various barred potentials.

3.1. *The fluid code*

The code is an second-order, flux-splitting Eulerian grid code for an isothermal gas in an imposed gravitational potential representing the stellar component and halo of the Galaxy. We neglect the self-gravity of the gas in order to reduce computational requirements. We justify this omission on the grounds that the gas surface density is considerably less than that of the stellar bulge and disk, especially in the inner regions of the Galaxy with which we are primarily concerned (see Section 5.1 below).

Our grid has 200 by 400 cells, each 50 pc square, and we enforce a 180° rotation symmetry, so that the grid is effectively 400 by 400. The grid is fixed with respect to the barred potential, and both rotate at a steady pattern speed; the bar is aligned at 45° to the grid axes. The time step is variable, chosen automatically via a Courant condition, and is generally approximately 0.1 Myr. The sound speed of the gas is taken to be 8 km s^{-1} (cf. Gunn *et al.* 1979), corresponding to a temperature of $\sim 10^4$ K. Varying the sound speed within reasonable limits of a few km s^{-1} does not materially affect the derived gas flow.

By its nature, the code approximates the interstellar

medium as an Eulerian fluid, smooth on scales of the grid cell size. Without some idealization it is hopeless to simulate the extremely complex dynamics of the multiphase ISM, which has structure on all observed scales and a vast assortment of energy inputs and outputs. Some authors (Jenkins & Binney 1994; Combes 1996) have suggested that smooth-fluid models using the Euler equations, such as grid codes and smooth-particle hydrodynamics, are not appropriate for the clumpy ISM, and have advocated various sticky-particle methods. Sticky-particle codes may be well suited to simulating the dynamics of the self-gravitating molecular cloud component, which Jenkins & Binney implicitly probed by comparing to CO observations. However, the H I in the neutral ISM is much less clumpy; it is not clear that the neutral ISM is made up of discrete clouds, especially over scales of $\gtrsim 50$ pc, the grid scale we use. Essentially, applying the Euler equations to the ISM simply asserts that the ISM has a pressure or sound speed defined in a coarse-grained sense, over scales greater than the code's resolution.

Englmaier & Gerhard (1997) used an SPH code to simulate flow in one of the model potentials that Athanassoula (1992b) used with the Eulerian grid code. For equivalent input parameters, Englmaier & Gerhard obtained results very similar to Athanassoula's, which reassures us that the simulations are not dependent on the fluid-dynamical algorithm.[1]

A limitation of particle codes is their inability to represent large density contrasts. By design, spatially adaptive particle codes resolve structure well in high density regions, but the finite number of particles precludes adequate representation of the fluid properties in very low density regions. Grid codes, on the other hand, cannot resolve spatial structure below a few grid cells, but can handle nearly any density contrast with no increase in overhead, and represent low and high density regions equally. In a case such as the gas in the Milky Way bar, where the geometry and scales of interest are largely fixed by the stellar potential, spatial adaptivity is less essential and grid codes are generally more efficient. The grid's advantage in density contrast is especially important since the gas in low density regions will prove crucial to match the observed emission in the forbidden quadrants of the $\ell - V$ diagram, as discussed further in Section 5.2.

3.2. *Simulation procedure*

We begin each simulation in a quasi-equilibrium state, with the mass of the bar redistributed in an axisymmetric configuration, the gas on circular orbits, and a uniform gas surface density of 5 $M_\odot$ pc^{-2}. We turn on the bar by linear interpolation between the initial axisymmetric state and its fully barred shape, reaching its final state in 0.1 Gyr. The bar growth time is approximately equal to the orbital period at a radius of 3 kpc. Different choices for the growth time and initial density do not particularly affect the results, save that the final gas density distribution scales overall proportionally to the constant chosen for the initial density.

We continue the simulation to 0.2 Gyr to allow the gas flow to "settle" after the bar has grown, and to 0.3 Gyr to verify that the flow has stabilized. The gas response can never reach a completely steady state, because the gas inside co-rotation continuously loses energy in shocks and flows toward the center.[2] Gas continues to accumulate in the center, but there is very little change in the gas velocity field from 0.2 to 0.3 Gyr.

We use the gas density and velocity fields at 0.2 Gyr to construct $\ell - V$ diagrams as would be seen by an observer in the plane of the simulation. The observer is placed 8.5 kpc from the Galactic center and in the LSR, moving with a velocity of $\Theta_0 = 220$ km s^{-1} toward $\ell = 90^\circ$, and at a given viewing angle – the angle between the bar major axis and the Sun-Galactic Center line. (The effect of a different LSR motion is discussed below in Section 6.2). The viewing angle is varied to find the best value, as detailed below in Section 4.2.

For each cell in the simulation grid, we calculate the longitude of the cell and the angle it subtends, and the radial velocity of the gas in the cell. The gas density in the cell and its distance from the Sun determine the observed brightness. The brightness distribution is convolved and sampled in longitude to model the angular beamwidth of the telescope and the 0.5° sampling of the observed positions, and convolved in velocity to include the effects of the sound speed of the gas ($c_s = 8$ km s^{-1}) and the velocity resolution of the observations (smoothed with a Gaussian of $\sigma = 5.5$ km s^{-1}).

3.3. *Model gravitational potentials*

Our models for the gravitational potential are similar to those used by Athanassoula (1992a,b). They have three components: an ellipsoidal bar, a centrally concentrated bulge, and an extended component to represent both the disk and halo.

We model the bar as a prolate Ferrers $n = 1$ ellipsoid with semimajor axis a and semiminor axis b. The bar density is given by

$$\rho(x,y,z) = \begin{cases} \rho_{0,\mathrm{bar}}\,(1-u^2) & \text{if } u^2 < 1, \\ 0 & \text{if } u^2 > 1, \end{cases} \qquad (1)$$

where

$$u^2 = \frac{x^2}{a^2} + \frac{y^2}{b^2} + \frac{z^2}{b^2}. \qquad (2)$$

This model for the bar is convenient because its gravitational field is analytic (Binney & Tremaine 1987), but it is a crude model for the real bar (*e.g.* Dwek *et al.* 1995). We compensate for one of its principal weaknesses by adding a bulge component. Ferrers bars are not very centrally concentrated; the bulge component allows us to increase the central concentration and to adjust its strength relative to the bar. The bulge is a modified Hubble profile sphere

[1] Englmaier & Gerhard found that increasing the sound speed of the gas to 20–25 km s^{-1} changed the flow pattern. However, such a large value implies an unreasonably high temperature for the ISM, and is inconsistent with the value found by Gunn *et al.* (1979).

[2] The gas build up in the center can be significant if the code is run for many rotation periods, *e.g.* several Gyr. This effect can be lessened by the use of a "gas-recycling" provision in the code. However, we found that gas recycling caused long-period oscillations in the flow with the fine grid used here, probably because it redistributes energy over the grid (G. van Albada, private communication). The oscillations do not occur on coarser grids, such as those used by Athanassoula (1992b), presumably due to the higher numerical diffusivity. Since we are not interested in the long-term evolution of the flow, we avoid this numerical problem by turning gas recycling off.

with core radius r_c and density given by

$$\rho(r) = \rho_{0,\rm bul} \left[1 + \left(\frac{r}{r_c}\right)^2\right]^{-3/2} . \quad (3)$$

The "bulge" component can be viewed as effectively part of the bar; our treatment of the two as separate analytical components does not imply that we regard them as distinct, either photometrically or kinematically. We use $M_{\rm bul}$ to refer to the bulge mass within 1 kpc of the Galactic center, since this is most analogous to the central concentration of the bar; the *total* mass of a modified Hubble profile sphere diverges at large radii.

The extended component has the potential

$$\Phi(R) = \Phi_0 \ln\left(1 + \sqrt{1 + (R/R_c)^2}\right), \quad (4)$$

where R_c is scale length. If all the mass that gives rise to this potential were to reside in the disk, it would have the surface density of a Rybicki disk (given by Zang 1976 and derived independently by Hunter, Ball & Gottesman 1984):

$$\Sigma(R) = \Sigma_0 \frac{R_c}{\sqrt{R_c^2 + R^2}}, \quad (5)$$

with $\Phi_0 = 2\pi G \Sigma_0 R_c$. The rotation curve of this potential becomes asymptotically flat at large radius, making it suitable for modeling the contribution both of the axisymmetric part of the stellar disk and of the dark matter halo.

As the simulation is two-dimensional, it is insensitive to the three-dimensional forms of these density distributions; any distribution that yielded similar forces in the plane could be substituted. Thus, mass can be traded off between the axisymmetric components; for example, it is unimportant that the density of the Hubble bulge falls off slowly, since the small additional contribution to the rotation curve (cf. Figure 3) could be absorbed into the rotation curve of the disk or halo.

The total potential is specified by seven parameters: a central density and scale length for each of the bulge and "disk," and a central density and two axis lengths for the bar. Our only constraint is that the rotation curve should be roughly flat outside R_0, with a circular velocity from 200–220 km s^{-1} at 8.5 kpc. An eighth parameter, the Lagrange or corotation radius R_L, is required to fully specify a model; choosing R_L is equivalent to specifying a pattern speed for the bar. The gas flow pattern is determined by the adopted potential, but the $\ell - V$ diagram further depends on the viewing angle $\phi_{\rm LSR}$ between the Sun–Galactic center line and the major axis of the bar.

We varied the parameters by trial and error and examined the $\ell - V$ diagrams after each run to learn the effects of changes in bar size, bar mass, bulge mass, Lagrange radius and so on. Our goal was to find a model or models that matched the observations reasonably well, rather than systematically to explore the parameter space, which is impractical given the large number of parameters. We did run some series to explore the effect of varying a parameter, most notably, varying the Lagrange radius while holding all other parameters constant.

In all, we ran 51 models; their parameters are given in Table 1. The table is sorted by the goodness of fit as measured by the RMS deviation in velocity between model and data (discussed further in Section 4.2). The best fit viewing angle and the goodness of fit are tabulated in the last two columns of Table 1. The models are numbered best to worst; the number, naturally, does not correspond to the order in which the models were run, since we improved the models by learning from past results – Model 1 was actually the 46th model run.

4. COMPARISON TO OBSERVATIONS

We compared the outer envelope – the extreme-velocity contour – of the synthesized $\ell - V$ diagrams to that of the data. The observed EVC used is the contour of 0.125 K degrees of antenna temperature summed over b, or 1.25 $\rm M_\odot\,kpc^{-2}\,deg^{-1}\,/\,km\ s^{-1}$ of atomic gas (H and He), using the calibration given by Liszt & Burton (1980). The data points used are shown by the filled circles in Figure 1. As discussed in Section 2, those portions of the EVC that show signs of contamination from foreground disk emission are excluded from comparisons to models.

4.1. *The EVC contour level*

The position of the observed extreme-velocity contour is determined by the actual terminal velocity envelope of the gas, extended by the velocity broadening due to the gas sound speed and the instrumental resolution. Since the flux level at which the EVC can be observed is also limited by the noise in the observations, the EVC is not an intrinsic property of the Galaxy, but also depends on the observational parameters. In the tangent-point method, the observed EVC must be corrected to yield the terminal velocity envelope. In practice, it is conventional to assume that (1) the difference between the terminal velocity $v_t(\ell)$ and the EVC is some constant ΔV, and (2) ΔV can be determined by observations near $\ell \simeq \pm 90°$, where the actual terminal velocity is expected to be zero (cf. Gunn *et al.* 1979).

As the data we are using do not cover $\ell \simeq \pm 90°$, we cannot make use of this method to derive ΔV. In order to compare the observations and simulations, we have constructed simulated $\ell - V$ diagrams which take into account the velocity dispersion of the gas and the instrumental resolution. But the absolute level at which to place the EVC in the simulated $\ell - V$ diagram is not constrained, since we do not know ΔV for the observations. Fortunately, both simulated and observed $\ell - V$ diagrams have fairly sharp edges, in the sense that the flux falls off rapidly with increasing $|V|$ – see Figures 1 and 4. The lowest contours simply trace the falloff profile of the velocity dispersion and instrumental resolution. We compared simulated $\ell - V$ diagrams to that observed, examining the fall off at the edges of the distribution, to set the level for the EVC in the simulated $\ell - V$ diagram. Placing the EVC at ~ 1.7 $\rm M_\odot\,kpc^{-2}\,deg^{-1}\,/\,km\ s^{-1}$of total simulation gas produced a reasonably good match but EVC levels of 1.25 – 2.5 $\rm M_\odot\,kpc^{-2}\,deg^{-1}\,/\,km\ s^{-1}$ were almost equally acceptable.

Because the $\ell - V$ diagrams do have sharp edges, changing the flux level of the comparison EVC, even by a factor of 2, does not have a strong effect. We ran comparisons of the entire series of models at EVC contour levels from

$0.625 - 5.0\ M_\odot\ kpc^{-2}\ deg^{-1}\ /\ km\ s^{-1}$ and verified that the small changes caused by different choices for the EVC level produce only minor changes in the rank ordering of models, and do not affect our conclusions.

We note that comparing the simulation EVC at $1.7\ M_\odot\ kpc^{-2}\ deg^{-1}\ /\ km\ s^{-1}$ of total gas to the observed H I EVC at $1.25\ M_\odot\ kpc^{-2}\ deg^{-1}\ /\ km\ s^{-1}$ of atomic gas could be interpreted to mean that the gas is 75% atomic; levels of $1.25 - 2.5\ M_\odot\ kpc^{-2}\ deg^{-1}\ /\ km\ s^{-1}$ would imply atomic fractions of 100% – 50%. However, the comparison is not reliable for this purpose. The edges of the EVC largely represent gas in low density regions, and the molecular fraction is undoubtedly higher in high density regions – CO emission does not generally extend to the velocities of the H I EVC (Dame *et al.*1987). Additionally, the inferred fraction would be changed if the value of the initial gas surface density used in the simulations were changed. It is, however, comforting that the inferred atomic fraction is close to but less than 1. (The actual atomic mass fraction in the inner Galaxy is perhaps 50%; cf. Bronfman *et al.* 1988; Bloemen *et al.* 1986.)

4.2. *Best fit and viewing angle*

To rank the models by the quality of their fit to the data, we compute the root-mean-square deviation in velocity between the location of the simulated EVC and the observed data points. The RMS velocity deviation is not an "error" in a statistical sense; it serves as a figure-of-merit for ranking the models. The RMS places a relatively high weight on large deviations, which penalizes gross differences between model and data more than large numbers of small differences.

For a given model, the position of the observer with respect to the bar must be specified to construct an $\ell - V$ diagram. We define the "viewing angle" $\phi_{\rm LSR}$ to be the angle between the bar major axis and the Galactic Center–to–Sun line, so that 0° is an end-on bar, 90° is side-on, and values between 0° and 90° put the near end of the bar in the first Galactic quadrant ($0° < \ell < 90°$). We determined the best-fit viewing angle for each model iteratively by synthesizing $\ell - V$ diagrams and computing the RMS deviation at viewing angle intervals of 10°, 4°, and 1°, successively, narrowing the search interval at each step. The best-fit viewing angle for each model and the corresponding RMS velocity deviation are tabulated in Table 1, sorted by the goodness of fit. The viewing angle given is for the best fit between 0° and 90°; these are the realistic models since many lines of evidence place the near end of the bar in this quadrant. For the few models that have a better fit outside this quadrant, that result is given in the table footnotes.

5. RESULTS: I. THE BEST MODEL

5.1. *Properties of the model*

Our primary result is that we have found a model which reproduces the outer contour of the $\ell - V$ diagram fairly well. This model is model 1 in Table 1; a number of the models that are runners-up are closely related to it. Model 1 has a bar with semimajor axis 3.6 kpc and Lagrangian radius 5.0 kpc, corresponding to a pattern speed of 41.9 $km\ s^{-1}\ kpc^{-1}$. The best-fit $\ell - V$ diagram is shown in Figure 4 and the RMS velocity deviation is $16.54\ km\ s^{-1}$. The minimum in RMS deviation is well localized at a viewing angle of 34° to the bar major axis, although changes of a few degrees ($< 5°$) are possible without greatly worsening the fit. The localization in RMS deviation is similar for all of the better models. The effects of changes in the viewing angle are discussed further in Section 6.

Figure 5 shows the surface density distribution of the combined bar, bulge, and disk+halo components, as projected along the z axis of the Galaxy. The figure shows the central 8 kpc by 8 kpc region of the model, in what is essentially a face-on view – although the contours are in surface density of mass, not light. This plot demonstrates the influence of the bulge component, which makes the central concentration of the bar much higher than that of a Ferrers bar in isolation. It is also clear that the full surface density distribution is less elongated than the bar component alone, with an axis ratio of about 3:1 as compared to the bar component's axis ratio of 4:1.

When the mass density is integrated over $-100 < z < 100$ pc, the lower estimate for the thickness of the gas layer, the resulting distribution is similar to that of Figure 5 but with mass surface density lower by a factor of about four. Within this range of z, at the bar end the mass surface density is 140 $M_\odot\ pc^{-2}$; in the central region at $R < 0.5$ kpc the mean mass surface density is 2900 $M_\odot\ pc^{-2}$. A comparison of these mass surface densities with the gas surface density suggests our neglect of gas self-gravity is justified.

The gas density in the innermost 8 kpc square of this model is shown in Figure 6, also in a face-on view. The long, straight high density features in the bar are shocks, with transverse velocity jumps of $\sim 200\ km\ s^{-1}$, extending out to 2.9 kpc from the galactic center. They are parallel but offset from each other; near the center the straight shocks join onto an oval or nuclear ring of high density gas that is also the location of shocks. The semi-major axis of this oval is 0.5 kpc. The gas surface density in the shocks is 5–20 $M_\odot\ pc^{-2}$; within $R < 0.5$ kpc the mean gas surface density is 130 $M_\odot\ pc^{-2}$. The straight, offset shocks and the inner oval are characteristic of gas flow in strongly barred potentials with an inner Lindblad resonance (Athanassoula 1992b).

Dust lanes with morphologies similar to the high density gas in Figure 6 are observed in many barred galaxies. The dust lanes are presumably caused by the high gas density at the shock (Prendergast 1962, unpublished; see also van Albada & Sanders 1982; Prendergast 1983; Athanassoula 1992b). Spectroscopy of barred galaxies shows sharp velocity jumps at the location of the dust lane (*e.g.* Pence & Blackman 1984; Lindblad *et al.* 1996; Regan, Vogel & Teuben 1997; Weiner *et al.* 1999).

Figure 6 also shows that there is little gas in the lens region of the galaxy, inside 3 kpc; barred galaxies often show a central hole in the gas distribution swept clear by the angular momentum transport of the bar (*e.g.* NGC 1300, England 1989; NGC 1398, Moore & Gottesman 1995; and NGC 4123, Weiner *et al.* 1999). Outside 3 kpc, the gaseous disk is relatively quiescent; the bar does not drive a large response in the outer disk. The disk does not exhibit spiral patterns outside the bar radius; spirals in the outer disk could be driven by spirals in the stellar disk and/or the self-gravity of the gas, which we have neglected in order to concentrate on the inner Galaxy.

The gas velocity field as seen in a non-rotating frame,

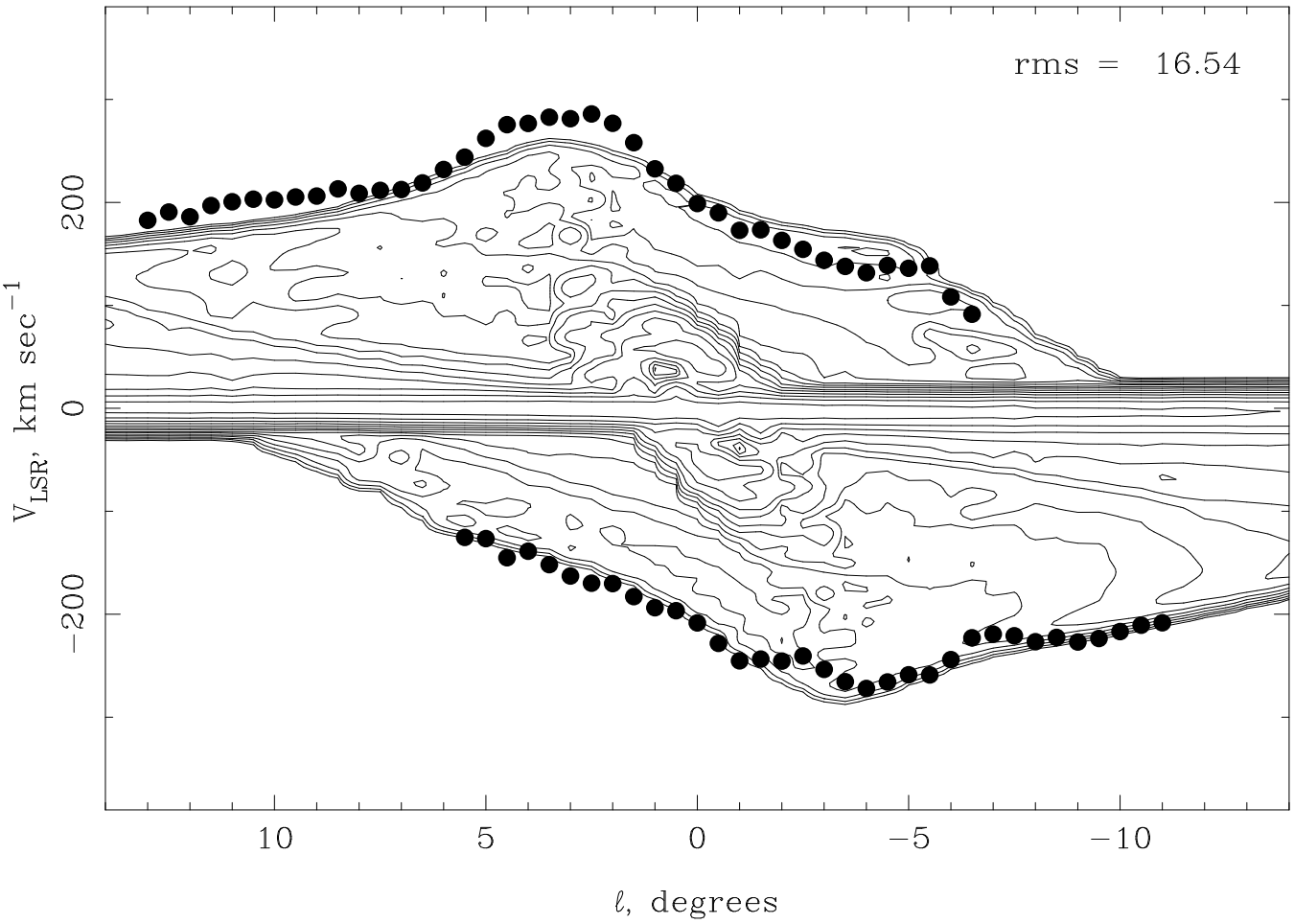

FIG. 4.— The $\ell - V$ diagram for the best-fitting model, Model 1, as viewed at 34°. The lowest contour is 1.7 $M_\odot$ kpc^{-2} deg^{-1} / km s^{-1} of total gas and the contours increase geometrically by a factor of 2. The filled circles are the observed data points. The RMS velocity deviation between model and data is 16.54 km s^{-1}.

in the inner 8 kpc × 8 kpc region, is shown in Figure 7. For clarity, we have plotted only every fourth cell. The velocity changes abruptly at the shocks along the density peaks. Essentially, gas in the bar moves up to the shock at relatively high velocity and hits the shock, dissipating energy. The post-shock gas then streams back down the bar, gaining velocity quickly as it moves away from the shock and falls down the potential well.

Gas streamlines in the bar are elongated along the bar, in the manner of the x_1 family of stellar orbits in bars, but are clearly not symmetric about the major axis of the bar, unlike the x_1 orbits. The shocks are located along the leading edge of the streamlines and are approximately parallel to the bar; the major axis of the elongated streamlines is rotated approximately 5° ahead (toward the leading side) of the bar major axis. This angle, which we will refer to as the "lead angle," is closely related to the pattern speed of the bar, to be discussed further in Section 6.3.

Near the center of the bar, the major axes of the streamlines change, so that the streamlines are elongated across the bar more than along it, similar to the x_2 family of stellar orbits present in bars with inner Lindblad resonances (Athanassoula 1992a,b). The central oval of high gas density corresponds to this family of streamlines. Again, the streamlines are rotated by an oblique angle with respect to the bar, unlike the x_2 stellar orbits, which are perpendicular to the bar major axis.

5.2. *Inverting the projection into $\ell - V$ space*

The plot of the gas streamlines offers some understanding of the features in the $\ell - V$ diagram, but the effect of projection into $\ell - V$ space is much clearer in Figure 8. This figure plots the radial velocity observed in Model 1 as a function of position on the grid, i.e. over the plane of the Galaxy, showing the radial velocity *before* it is projected into the $\ell - V$ diagram.

The gas at forbidden velocities moves toward the Sun at $\ell > 0°$, the side where most of the gas is moving away, and vice versa at $\ell < 0°$. It is clear from Figure 7 and Figure 8 that forbidden velocities belong to low-density gas approaching the shocks. The preshock region with forbidden velocities extends all the way out to the shock tip at 2.9 kpc. However, the magnitude of the forbidden radial velocities in the preshock region falls below 100 km s^{-1} at about 1.5 kpc from the Galactic center, which corresponds roughly to $\ell = \pm 6°$ for the viewing angle of 34°. Past this point, emission at forbidden velocities is obscured in the Milky Way by the band of emission from foreground gas.

Identifying the emission in the forbidden quadrants with the low-density preshock gas may explain why the forbidden emission is much more extensive in H I than in

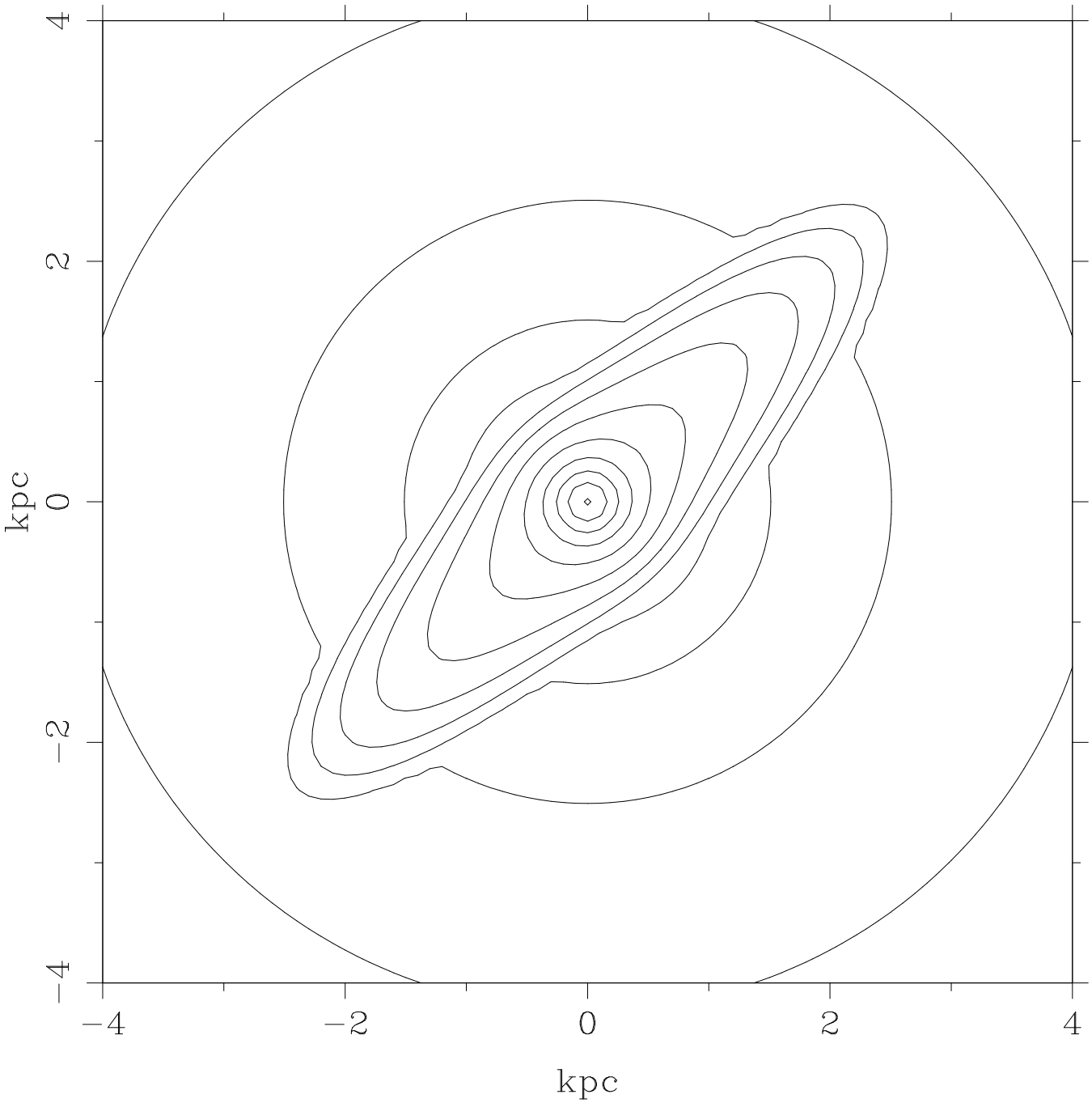

FIG. 5.— The face-on surface density of the mass distribution for Model 1, as projected along the z-axis, and shown for the innermost 8 kpc by 8 kpc of the Galaxy. The lowest contour is at 400 $M_\odot$ pc^{-2}, and the contours increase geometrically by a factor of $\sqrt{2}$.

CO, while the peaks in the H I $\ell - V$ diagram, which come from higher density regions, are present in the CO $\ell - V$ diagram. The identification of forbidden velocities with the preshock gas also illuminates some of the difficulty Jenkins & Binney (1994) had matching their sticky-particle models to the data. The $\ell - V$ diagrams they presented have very little emission in the forbidden quadrants. However, their maps of gas density in the plane of the simulation show that the apparent lack of emission is because there are very few particles in the preshock regions at any given time, as discussed in Section 3.

The high and narrow peaks in the EVC at $\ell \sim +3°$ and $-4°$, or ~ 0.6 kpc projected distance from the Galactic center, have no counterparts in the equivalent axisymmetric model (Figure 2). The origin of these peaks can also be understood from Figure 7; the elongation of the orbits caused by the strong ellipticity of the gravitational potential results in high gas velocities roughly parallel to the bar major axis. The observed high radial velocities arise from the gas on elongated orbits just as it passes the oval of high-density gas (Figure 8). The EVC declines rapidly beyond the peak because the gas at larger radii does not fall as deeply into the bar's potential well, and is on less elongated orbits.

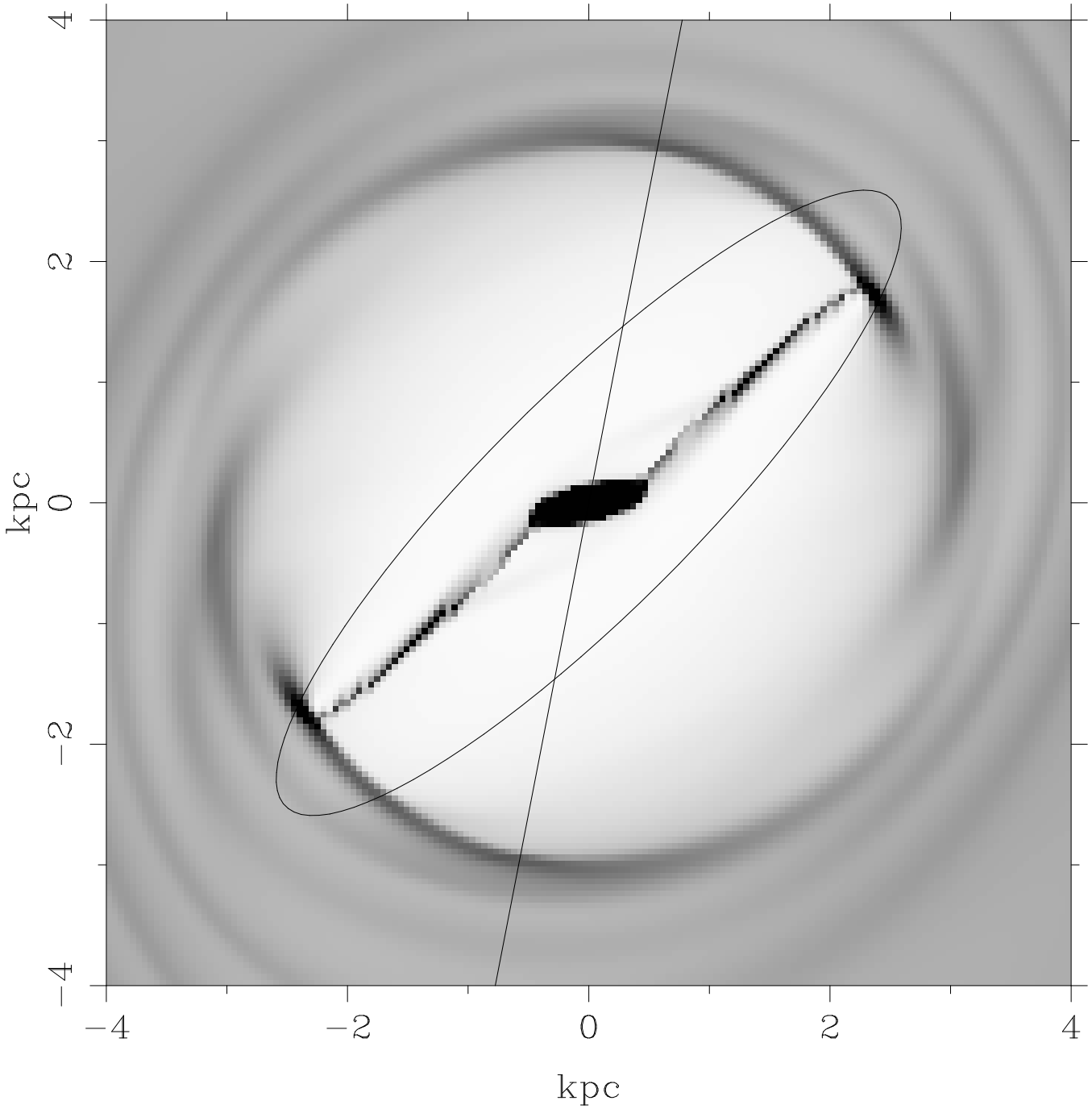

FIG. 6.— The face-on gas density in the innermost 8 kpc by 8 kpc of Model 1, as viewed from above the plane of the simulation. The grayscale runs from 0 to 15 $M_\odot$ pc^{-2} of total gas, with dark representing higher density. The bar is at a 45° angle to the grid, running from lower left to upper right. The ellipse represents the points at which the bar density drops to zero, with semimajor axis 3.6 kpc. The sense of the bar rotation is clockwise. The inclined line from top to bottom of the figure represents the Sun–Galactic Center line for the best-fit viewing angle of 34°, with the Sun above the top of the figure.

Many authors (e.g. Gunn *et al.* 1979; Gerhard & Vietri 1986; Liszt 1992; Burton & Liszt 1993) have noted that the peaks in the EVC and the rapid decline imply an unusual rotation curve if the gas is assumed to move on circular orbits; the inferred rotation curve also shows a sharp rise and rapid decline. These features are more naturally explained by gas flow in a triaxial potential (*e.g.* Gerhard & Vietri 1986, Burton & Liszt 1993). Simulations such as model 1 show that not only the EVC peaks, but also the forbidden emission, are accounted for by gas flows in a strong bar. As Burton & Liszt emphasize, comparisons with a derived rotation curve instead of the full $\ell - V$ diagram both embody incorrect assumptions about the inner Galaxy and discard valuable data from the forbidden quadrants of the $\ell - V$ diagram.

Figure 8 can also be used to determine the location within the plane of the Galaxy of a feature in the $\ell - V$ diagram, or an object whose longitude and radial velocity are known but whose distance is uncertain. For example, the 3-kpc expanding arm goes approximately

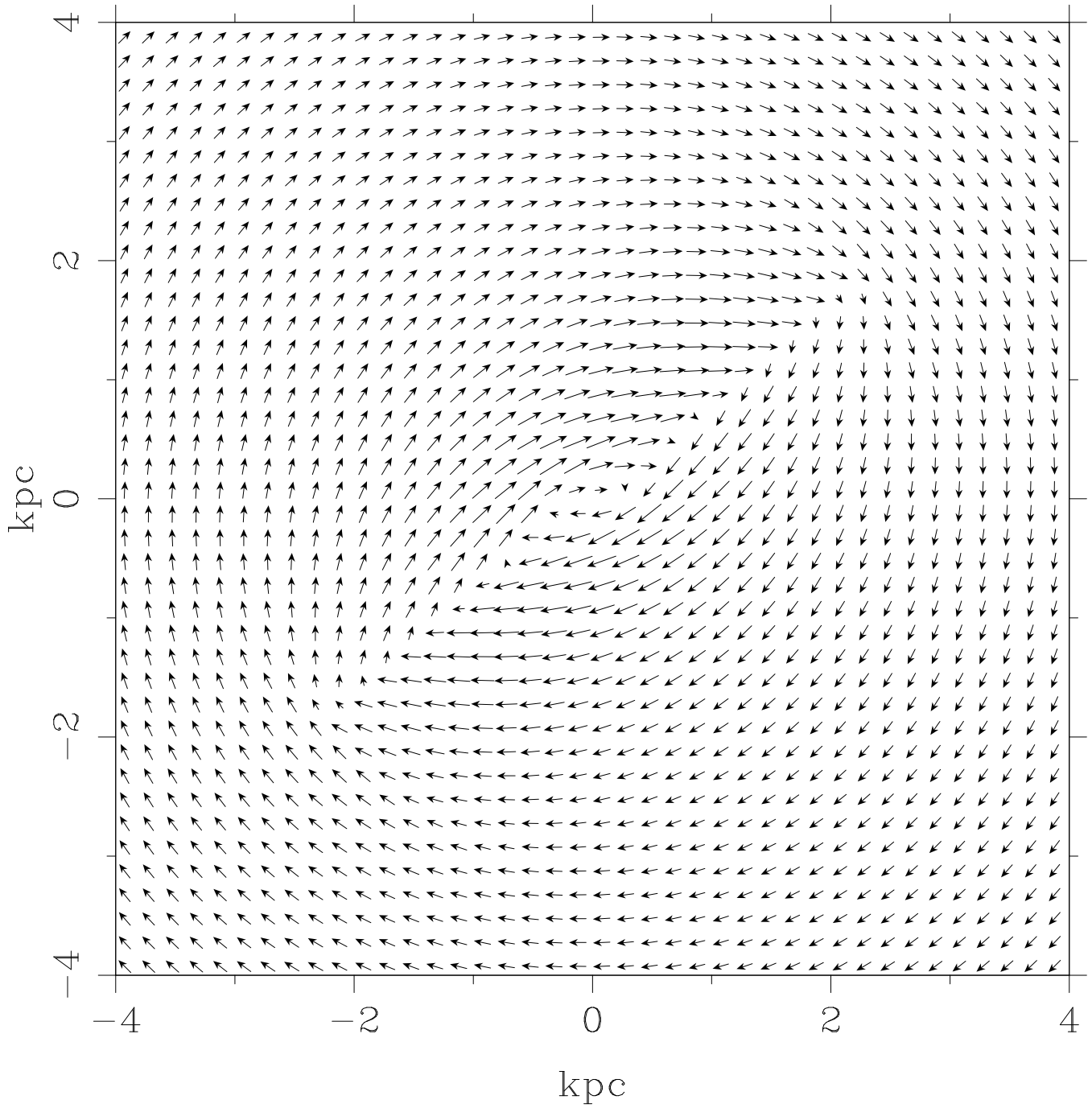

FIG. 7.— The gas velocity field in the innermost 8 kpc by 8 kpc of Model 1. The bar is at a 45° angle to the grid as before. For clarity, only every fourth cell in the grid is plotted.

through the points $(\ell, V) = (-10°, -100 \text{ km s}^{-1})$, $(-5°, -75 \text{ km s}^{-1})$, $(0°, -50 \text{ km s}^{-1})$, $(+2.5°, -35 \text{ km s}^{-1})$ (Liszt & Burton 1980). Locating these points on Figure 8 shows that they lie approximately on a arc centered on the Galactic center and of ~ 2.5 kpc radius, suggesting that the 3-kpc arm could be a spiral arm at about that radius with a small pitch angle, and that its motion is consistent with the overall Galactic velocity field, removing the need for large anomalous expansion velocities. In fact, an arm at approximately the right position is visible in Figure 6.

We note that even though the simulation is bisymmetric, the synthesised $\ell - V$ diagram has some asymmetry because one end of the bar is closer to the Sun than the other. The observed $\ell - V$ diagram is somewhat more asymmetric than the model, however. We cannot rule out the possibility that the observed asymmetry is due to actual asymmetries in the gas distribution or the shape of the Galaxy. However, the asymmetries in H I are considerably smaller than those in the CO $\ell - V$ diagram (Dame *et al.* 1987; Bally *et al.* 1988).

The most obvious deviation of this model from the observations is that it is not as strongly peaked at positive ℓ as the data, although this is essentially due to the asymmetry in the peaks of the data, since the model compromises

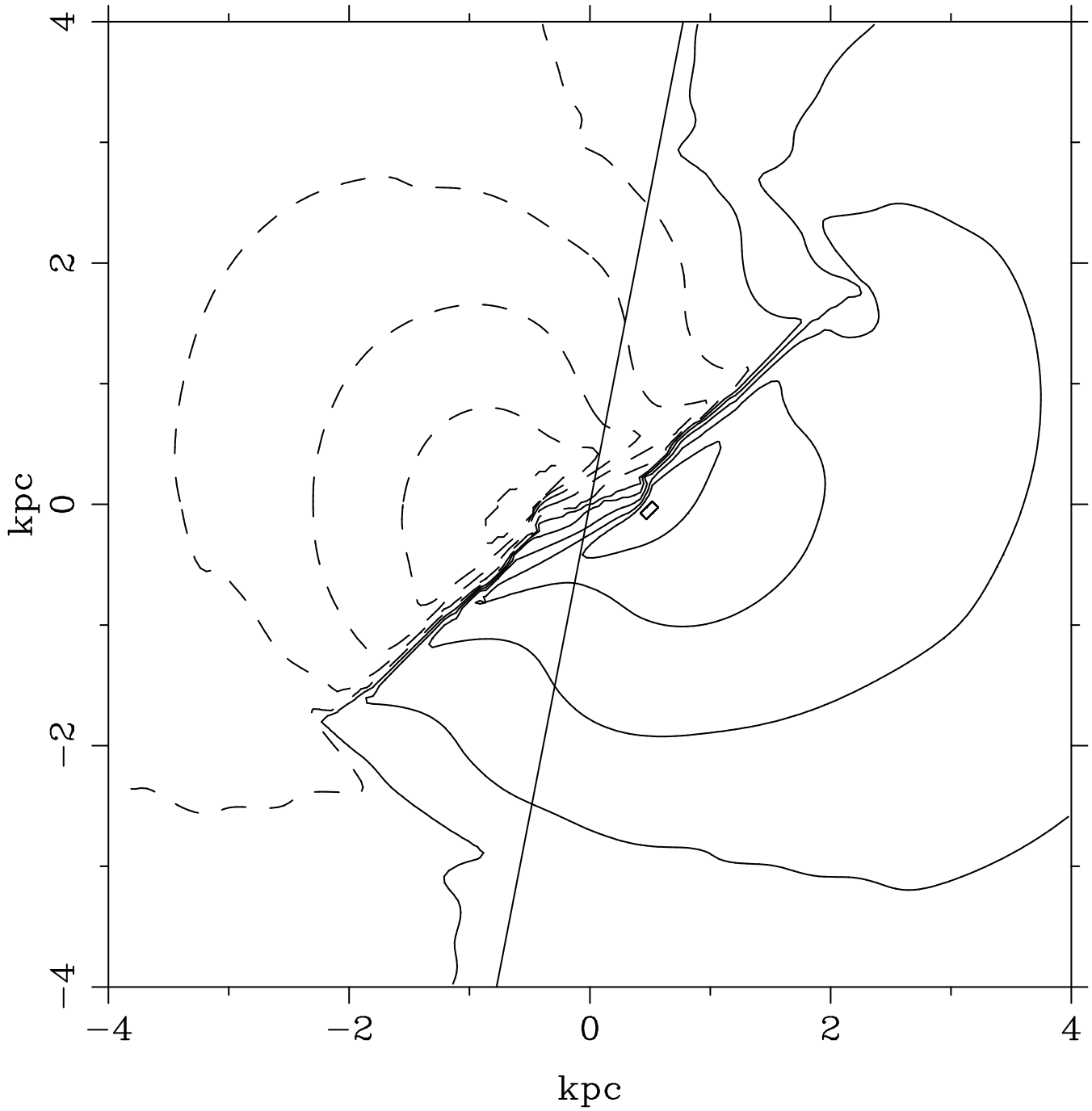

FIG. 8.— A contour plot over the inner 8 kpc $\times$ 8 kpc region of the radial velocity at which each grid cell in Model 1 is observed when the viewing angle is 34°. The contours are from –250 km s^{-1} to 250 km s^{-1} at intervals of 50 km s^{-1}; contours below zero are dashed. The bar is at a 45° angle to the grid, as before. The inclined line from top to bottom is the Sun–Galactic Center line ($\ell = 0°$), with the Sun above the figure.

by slightly overestimating the peak at negative ℓ. The model also produces a strong diagonal feature in the interior of the $\ell - V$ diagram from about (+3°, +100 km s^{-1}) to (–3°, –100 km s^{-1}) which is not present in Figure 1. This feature is caused by the nuclear ring of high density gas, which is not seen in the observations both because the gas is probably in the H_2 phase (cf. Rubin, Kenney & Young 1997) and because those parts of this feature with $|V| < 100$ km s^{-1} are obscured by the "main maximum" of foreground from disk gas.

The gas density and velocity fields in our model 1 are consistent with those observed in external barred galaxies. In particular, the straight shock regions with high gas densities can be identified with the straight dust lanes along the bar seen in many barred galaxies, which are generally thought to be the locations of shocks (Prendergast 1962, unpublished; see also *e.g.* Prendergast 1983; van Albada & Sanders 1982; Athanassoula 1992b).

Model 1 provides the best fit among our models, but it is by no means a unique solution to the problem of repro-

ducing the $\ell - V$ diagram. A slightly different choice of parameters could conceivably do better, and it is almost certain that some potential with components other than the particular analytic forms we used could improve on Model 1. However, the Galaxy is likely to resemble Model 1 in certain major respects, such as viewing angle, bar size, possession of an ILR, and high pattern speed. These conclusions are partly drawn from our experience with other, less well-fitting models, which we now discuss.

6. RESULTS: II. OTHER MODELS

In this section we describe other models to illustrate the influence of variations in some of the major parameters. This exercise allows us to infer the properties that a successful model is likely to possess in order to reproduce the observations.

A natural question to ask is whether the adverse consequences of changing one parameter can be compensated for by changes to other parameters. In general, the effects of the parameters are sufficiently interlinked that attempting to compensate by making one change has other unintended consequences. Given the number of parameters, it is impractical to test for all possible compensatory changes, but we do not believe that large variations in important parameters can be compensated away. Although Model 1 was one of the last models to be run, it is a close variant of Model 3, which we had tried much earlier (our 24th run); we tried a number of variations to improve Model 3 before actually succeeding. Our experience makes it seem unlikely that some other radically different model could fit equally well or better, but we cannot rule out the possibility.

6.1. *Changes in viewing angle*

Changing the angle from which Model 1 is viewed is not properly a different model for the potential, but can drastically change the resulting $\ell - V$ diagram. Figure 9 illustrates the systematic changes that occur when Model 1 is viewed at angles $-10°$, $-5°$, $+5°$, and $+10°$ from the optimum value of $\phi_{\rm LSR} = 34°$.

Viewing a model more nearly end-on than optimum, as in Figure 9(a) and (b), produces both higher peaks in the EVC and steeper declines from the peaks. It also reduces the extent of the gas in the forbidden quadrants, relative to the height of the peaks. Once again, reference to Figure 7 reveals the reasons for these changes.

In a more end-on view of the bar, the elongated orbits that produce the velocity peaks are projected more onto the line of sight of the observer, making the peaks higher. Counter to what might be expected, the peaks do not move significantly closer together in a more end-on view because the streamlines in this part of the flow are curved, and the region contributing to the peaks rotates somewhat. The curve of the streamlines is caused by the presence of an ILR, because the x_2 orbit family forces the elongated streamlines in the inner region of the bar away from the center. The more end-on view also means that the region with highly to moderately elongated orbits subtends a smaller angle, and so the fall-off with increasing $|\ell|$ is more rapid.

The relative deficiency of gas in the forbidden quadrants occurs because the shocks, and the preshock regions responsible for the forbidden emission, subtend a smaller angle when the bar is viewed more end-on. In the more end-on view, the projected components of the velocities of the preshock gas are larger, which compensates somewhat, but the slope of the decline in the EVC from the peaks into the forbidden quadrants is steeper. Clearly, the peaks could be lowered by reducing the central density of the model, but the more end-on view would then yield too little emission in the forbidden quadrants.

The effects of a more side-on view of the bar, as seen in Figure 9(c) and (d), are essentially exactly the opposite. The velocity peaks drop and their slope is gentler. The extent of the gas in the forbidden quadrants increases, but the lower projected velocities give a gentler slope to the EVC.

Gross variations in viewing angle, to the point where, for example, a model is viewed fully side-on at $\phi_{\rm LSR} \sim 90°$, can produce $\ell - V$ diagrams that deviate somewhat from these rules of thumb. For example, some models such as numbers 6, 9, 12, and 18 can produce high velocity peaks at side-on viewing angles because the innermost streamlines derived from x_2 orbits (approximately perpendicular to the bar) are viewed end-on. These models are of little practical interest, since a number of other lines of evidence rule out such large viewing angles – for example, a grossly side-on view cannot produce the magnitude offset between bulge stars at positive and negative longitudes, as shown by Stanek *et al.* (1997). (We note that models 6, 9, 12, and 18 are all slow bars in which $R_L \geq 2.4a$; see below.)

6.2. *Motion of the LSR*

The $\ell - V$ diagrams were constructed by assuming that the LSR is moving with a circular (tangential) velocity $\Theta_0 = 220$ km s^{-1} relative to the Galactic Center, with no radial motion. We tested the effect of assuming a different velocity of the LSR relative to the Galactic Center. A radial motion of –5 to +10 km s^{-1}, positive outward, can be accommodated; values outside this range significantly worsen the models' fit to the data. The best values of the radial motion are between 0 and +5 km s^{-1}. The fits are not sensitive to reasonable variations of the circular speed, since the data are near $\ell = 0°$; values of Θ_0 from 160 to 240 km s^{-1} were tested and yielded acceptable fits. Varying the LSR motion has a minimal effect on the relative ranking of the models.

The non-circular motion predicted by the models for gas at the solar position is small. For Model 1, the gas at the solar position has a tangential velocity of 211 km s^{-1}, and a radial motion of –0.7 km s^{-1} (inward). Model 1 has an outer Lindblad resonance (OLR) near the solar position, but the gas is on an essentially circular orbit. The OLR could have observable effects on the kinematics of stars in the solar neighborhood, in either mean velocity or dispersion. The nature of the effects is not simple to predict (cf. Kalnajs 1992, Kuijken & Tremaine 1992, Weinberg 1994); moreover Dehnen's (1998) analysis of Hipparcos data shows that the velocity structure of nearby stars is quite complicated.

6.3. *Varying the pattern speed*

We created a sequence of models including Model 1 to test the effect of varying the Lagrange radius or, equivalently, the pattern speed of the bar. The sequence in

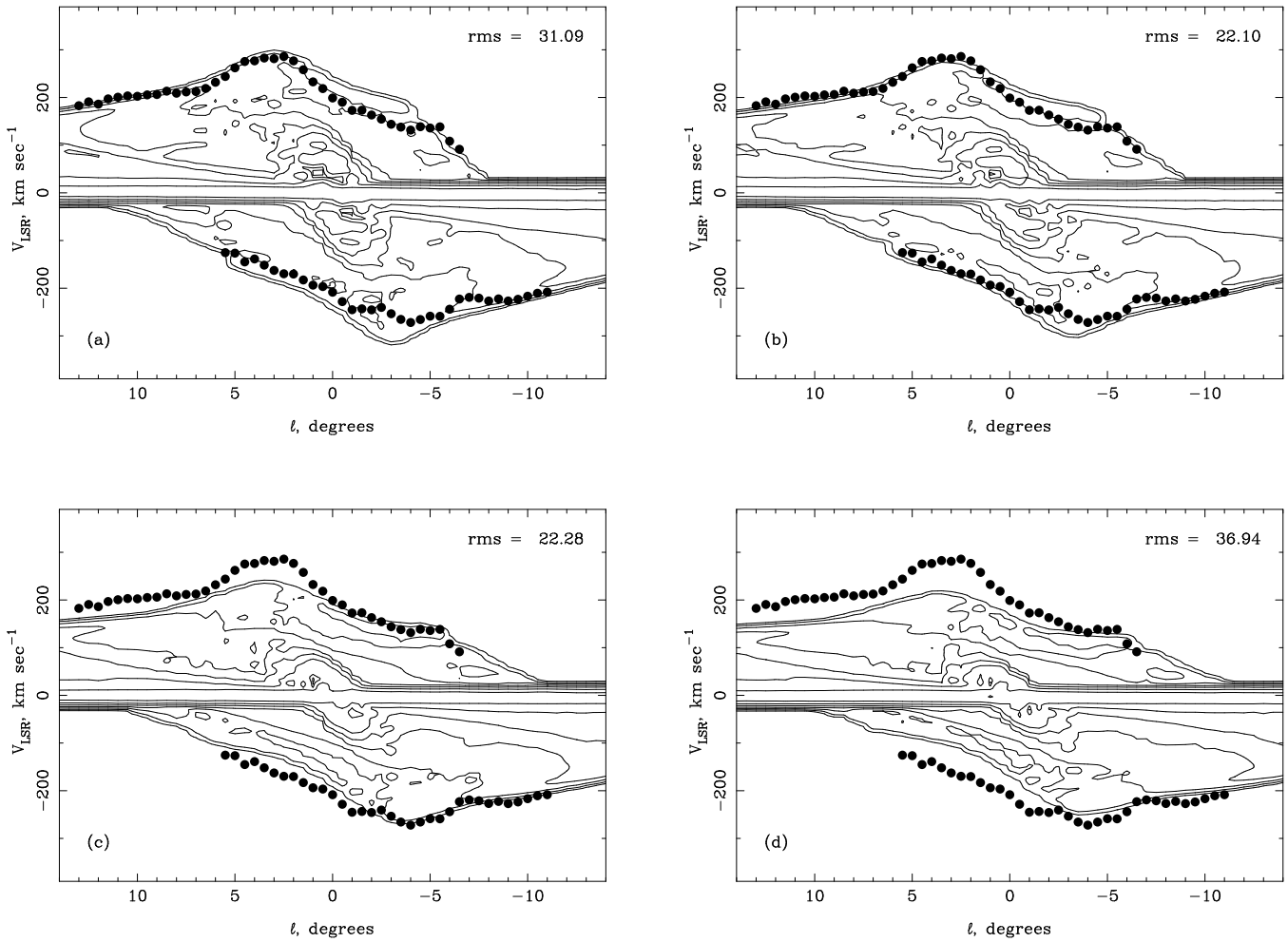

FIG. 9.— Longitude-velocity diagrams for Model 1 when it is viewed at angles other than the optimal viewing angle of $\phi_{\rm LSR} = 34°$. The lowest contour is 1.7 $M_\odot$ kpc^{-2} deg^{-1} / km s^{-1} of total gas and the contours increase geometrically by a factor of 4.
(a) $\phi_{\rm LSR} = 24°$, more end-on; RMS velocity deviation = 31.09 km s^{-1}.
(b) $\phi_{\rm LSR} = 29°$, RMS = 22.10 km s^{-1}.
(c) $\phi_{\rm LSR} = 39°$, more side-on; RMS = 22.28 km s^{-1}.
(d) $\phi_{\rm LSR} = 44°$, RMS = 36.94 km s^{-1}.

Lagrange radius R_L = 4, 5, 6, 7, and 8 kpc yielded models 2, 1, 5, 8, and 4 respectively. This sequence includes most of the best-fitting models (Model 3 is closely related).[3] Figure 11 shows face-on views of the gas density in this sequence of models, like that of Figure 6 for Model 1; Figure 10 shows $\ell - V$ plots for Models 2, 5, 8, and 4, to be compared with Figure 4.

The streamlines in Model 1 are not symmetric about the bar major axis; in fact the major axis of the streamlines is rotated by about 5° with respect to it, the "lead angle" referred to in Section 5.

Figure 11 shows that the lead angle increases with the Lagrange radius, as far as 25° for the slowest bar. The somewhat surprising result that several models with grossly different Lagrange radii and lead angles all appear to fit the $\ell - V$ data reasonably well arises because the models simply compensate by moving the best-fit viewing angle synchronously with the changes in the lead angle. The best-fit viewing angle stays roughly constant with respect to the *shocks*, which means that it also changes in a clockwise sense with respect to the bar, causing $\phi_{\rm LSR}$ to decrease. Thus changes in viewing angle are strongly coupled to the angle the gas streamlines make with the bar.

The systematic change in the location of the shocks has a relatively simple explanation. As the Lagrange radius is increased, the bar pattern speed slows (for R_L = 4.0, 5.0, 6.0, 7.0, 8.0, Ω_p = 54.2, 41.9, 34.9, 30.2, 26.6 km s^{-1} kpc^{-1} respectively). Inside the Lagrange or corotation radius, gas overtakes the gravitational potential well of the bar; the shocks are caused as the gas climbs out of the well, slows down, and piles up (Prendergast 1983). Although the shape of the gas streamlines is dependent on the full gas-dynamics, the magnitude of the velocity for gas at a given radius is roughly set by the gravitational acceleration from the mass interior to it, which is the same in all five models. In a frame co-rotating with the bar, if the bar is slower, the gas is moving faster as it overtakes the

[3]The groups of models {33, 26, 22, 6}, {23, 12, 9}, {19, 13}, and {21, 18} also comprise sets where only the Lagrange radius is changed – the effects are similar.

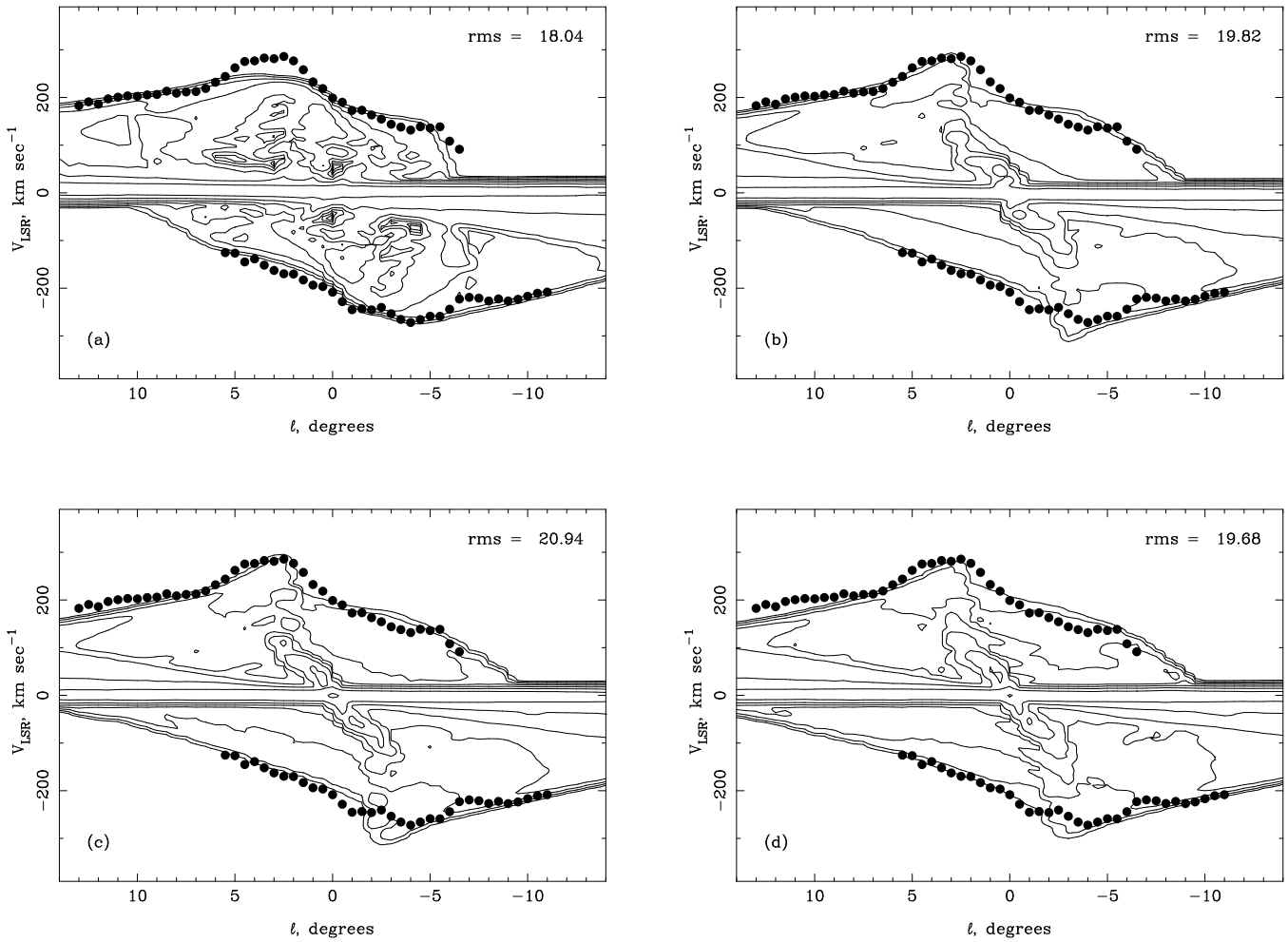

FIG. 10.— Longitude-velocity diagrams for a sequence of models with the same parameters as Model 1 except for the Lagrange radius. Model 1 (Figure 4) is between Models 2 (panel a) and 5 (panel b) in the sequence of increasing R_L. The lowest contour is 1.7 $M_\odot\,kpc^{-2}\,deg^{-1}\,/\,km\ s^{-1}$ of total gas and the contours increase geometrically by a factor of 4.
(a) Model 2, $R_L = 4.0$ kpc, bar viewing angle 31°.
(b) Model 5, $R_L = 6.0$ kpc, bar viewing angle 20°.
(c) Model 8, $R_L = 7.0$ kpc, bar viewing angle 15°.
(d) Model 4, $R_L = 8.0$ kpc, bar viewing angle 8°.

bar, so it climbs farther out of the potential well before the shock pile-up occurs. Therefore, in slower pattern speed models, the shocks are farther ahead of the bar, in the sense of more positive lead angle. The increased speed of the gas relative to the potential also increases the strength of the shocks.

The behavior of the shocks rules out slow bars, if we demand that the Milky Way bar should resemble bars in other galaxies. In external galaxies, the prominent dust lanes frequently seen along the bar run along the "leading" sides of the bar; the morphology of these dust lanes and exemplary galaxies are discussed by Athanassoula (1992b). Strong bars generally have straight dust lanes while weaker bars sometimes have curved dust lanes; in both cases, the dust lanes are generally parallel to the bar, as in the shocks of Model 1, or angled slightly in the sense of smaller lead angle. These dust lanes are identified with the high-density shocks, such as those in Figure 6, as discussed above. We know of no barred galaxies that have dust lanes with a lead angle of more than a few degrees; Athanassoula (1992b) argued that therefore strong bars rotate quickly. Merrifield & Kuijken (1995) have also showed that the bar in NGC 936 rotates quickly, via a completely independent method.

The position of the shocks in models 4 and 8 ($R_L = 7.0$ and 8.0 kpc), and in all other slow bar models we have run, is grossly inconsistent with what we know about barred galaxies. We reject these models for this reason, even though some of them formally fit the $\ell - V$ diagram well.

6.4. *Bar strength and shape*

The streamline plot of Figure 7 and the contours of observed velocity shown in Figure 8 suggest that the bar has to be strong and fairly elongated. Only a massive bar can produce the large non-circular motions needed to put gas at the forbidden velocities observed in the $\ell - V$ diagram. If the gas streamlines are less elongated than those seen in Figure 7, the regions with forbidden velocities are smaller and subtend a smaller range of Galactic longitude.

In our best model, the bar component has a mass of $M_{\rm bar} = 9.8 \times 10^9$ $M_\odot$, and the mass of the bulge compo-

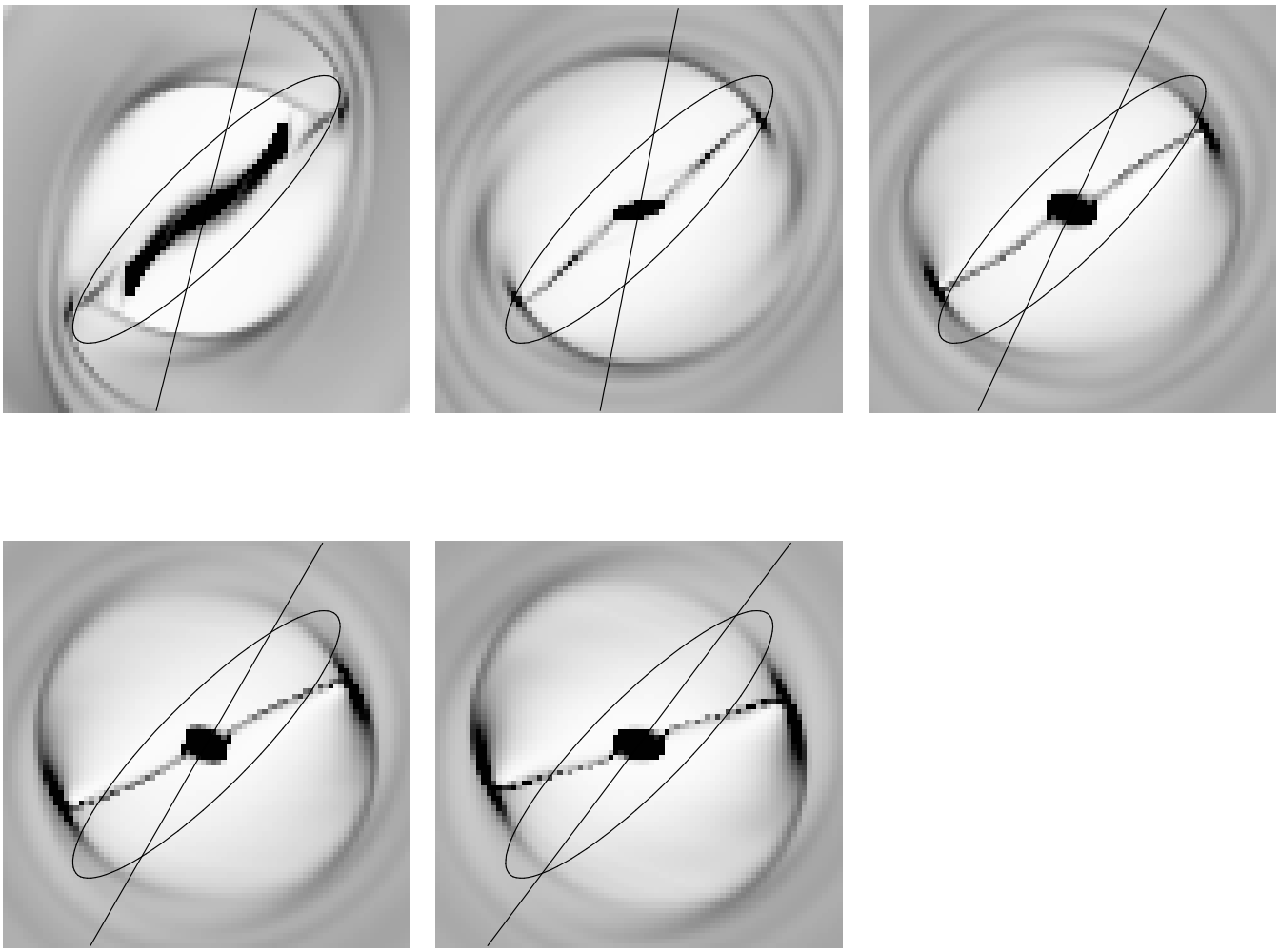

FIG. 11.— The gas density in the inner 8 by 8 kpc of the grid for a sequence of five models with different Lagrange radii and all other parameters fixed. The bar is at 45° to the grid in each model; the ellipse indicates the outer edge of the bar, at which the bar density drops to zero. The slanted line indicates the Sun–Galactic Center line for the best-fit viewing angle. The bar semimajor axis is $a = 3.6$ kpc.
(a) Model 2, $R_L = 4.0$ kpc. Shock lead angle $\approx 0°$, bar viewing angle 31°.
(b) Model 1, $R_L = 5.0$ kpc. Shock lead angle $\approx 5°$, bar viewing angle 34°.
(c) Model 5, $R_L = 6.0$ kpc. Shock lead angle $\approx 10°$, bar viewing angle 20°.
(d) Model 8, $R_L = 7.0$ kpc. Shock lead angle $\approx 15°$, bar viewing angle 15°.
(e) Model 4, $R_L = 8.0$ kpc. Shock lead angle $\approx 25°$, bar viewing angle 8°.

nent (within 1 kpc radius) is $M_{\rm bul} = 5.4 \times 10^9$ M$_\odot$.

The effect of a weaker bar on the $\ell - V$ plots is shown in Figure 12. Models 10, 11, 13, and 14 show a significant deficit of gas in the forbidden quadrants, notably at $\ell \sim -5°$. These models have smaller bars than Model 1 with lower M_{bar} (even though the bar density $\rho_{0,bar}$ is somewhat higher). Models 6, 9, and 12, which also have less massive bars than Model 1, do somewhat better at producing material in the forbidden quadrants, but only because the weaker forcing potential is partly compensated for by the stronger shocks that occur in a slow-rotating bar, as noted above. However, models 6, 9, and 12, like all the other slow-bar models, have shocks in an implausible position and are not viable models for the Galaxy.

The bar must also be strong in the sense of having a large axis ratio. The formal axis ratio of the Ferrers bar in Model 1 is 4:1, although the actual axis ratio of the total mass distribution, when the bulge and disk are included, is closer to 3:1 (cf. Figure 5).

Models with smaller axis ratios generally do not reproduce the data well. Figure 13 shows $\ell - V$ diagrams for several models whose bar components have axis ratios smaller than that of Model 1, with $a : b$ from 3.1:1 to 2.3:1. The axis ratios of the total mass distributions are fatter still. Although these models have different bar lengths, their appearance in $\ell - V$ diagrams is similar: they produce EVCs that are gently sloped, not sharply peaked as seen in the observations. In particular, the decline of the EVC away from the peaks is fairly sharp in the observations, but much too gentle in the models with low axis ratio bars.

Even an extremely centrally concentrated model but wide-barred potential such as Model 46, which has a small dense bulge, does not produce sharp peaks. More massive bars – longer, more dense, or both – do not successfully produce sharper peaks or better models: the most massive bars are models 45, 42, 37, 27, 43 and 44 ($M_{bar} = 41.2$, 27.2, 22.7, 17.5, 15.9, and 15.9 $\times 10^9$M$_\odot$, respectively).

As discussed above, the peaks in the $\ell - V$ diagram are

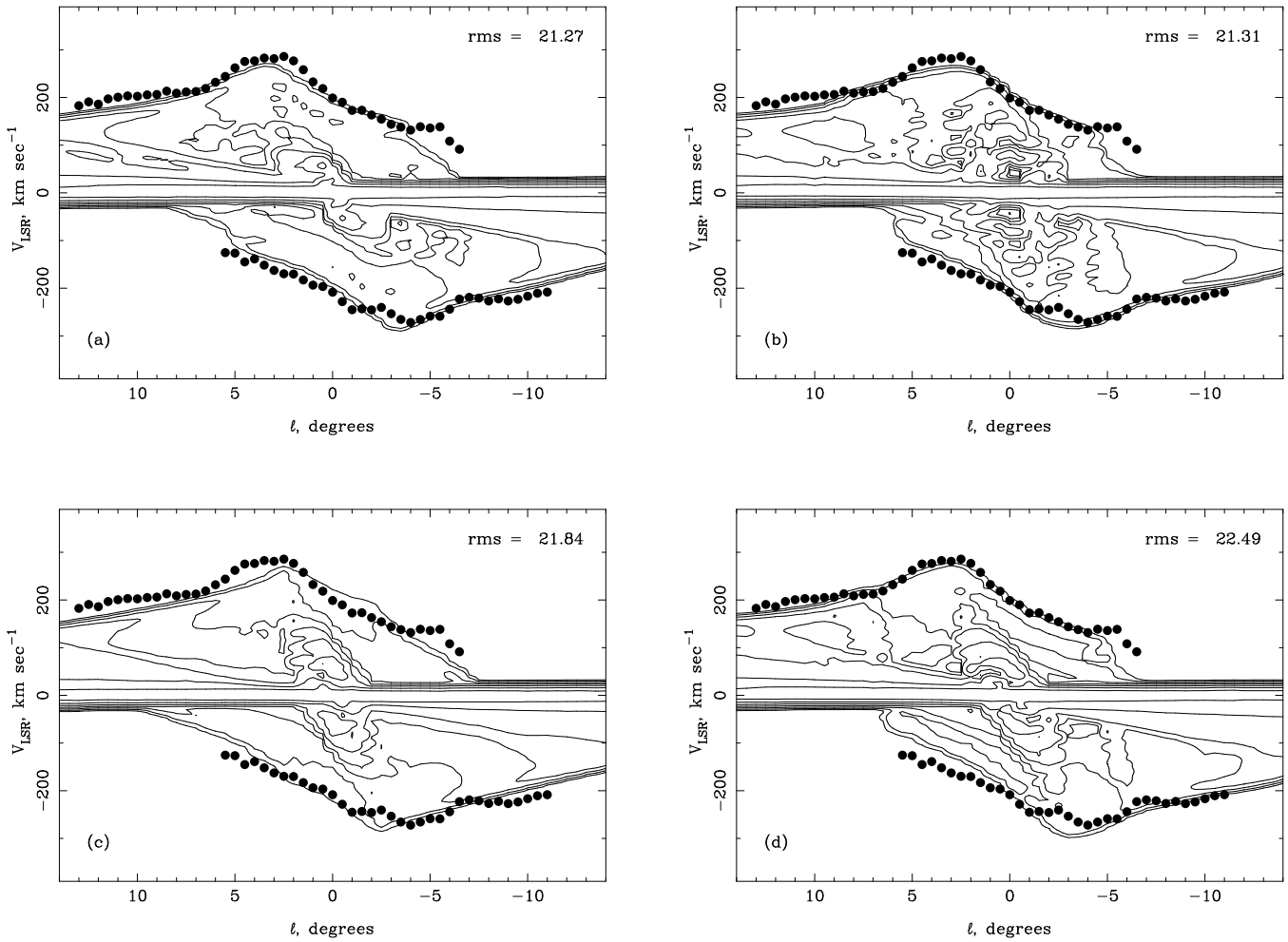

FIG. 12.— Longitude-velocity diagrams for several models with smaller bars of lower mass than that of Model 1. These models have M_{bar} = 80% that of Model 1, and M_{bul} between 75% and 125% that of Model 1. The lowest contour is 1.7 $M_\odot$ kpc^{-2} deg^{-1} / km s^{-1} of total gas and the contours increase geometrically by a factor of 4. There is a deficiency of gas in the forbidden quadrants in these models.
(a) Model 10, viewing angle 27°.
(b) Model 11, viewing angle 35°.
(c) Model 13, viewing angle 19°.
(d) Model 14, viewing angle 38°.

produced by the strongly non-circular motions inside the bar while the steep decline in the EVC as $|\ell|$ increases further is linked to the weakening of the non-circular motions as the quadrupole field decays quickly with Galactocentric distance. An axisymmetric model with an unusual mass distribution could be made to produce this behavior but could not, of course, give rise to forbidden velocities. A strong and elongated bar is favored to produce both forbidden velocities and the narrow peaks in the EVC.

6.5. *The presence of an inner Lindblad resonance*

As already noted, the peaks of the $\ell - V$ diagram arise from orbits just outside the oval of high density gas in the center, where the streamlines rotate to be highly angled to the bar rather than closely aligned with it. This rotation of the streamlines is related to the presence of an inner Lindblad resonance (ILR) (Athanassoula 1992a,b). Bars with an ILR have a family of stellar orbits near the center that are elongated perpendicular to the bar rather than along it, and the rotated streamlines are related to these orbits. Bars without an ILR have only streamlines elongated along the bar; these streamlines would yield peak gas velocities as they pass the center (Athanassoula 1992b).

An inner Lindblad resonance forces the elongated orbits away from the center, causing the highest bar-induced streaming velocities to occur some distance out, and producing sharply defined peaks in the $\ell - V$ diagram that are several degrees apart. If the bar did not have an ILR, the EVC peaks are not necessarily as sharply defined, nor can they be separated by several degrees in longitude, as is observed. Model 27 is the least centrally concentrated of all our models, and its best-fit $\ell - V$ diagram has EVCs without dominant peaks; the positive velocity EVC is nearly flat from $\ell = -3°$ to $\ell = 10°$. The least centrally concentrated potentials are models 27, 51, 45, 50, 48, and 42 (M_{bul}/M_{bar} = 0.019, 0.096, 0.11, 0.13, 0.16, and 0.17 respectively). Figure 14 shows $\ell - V$ diagrams for four of these weakly-concentrated potentials, which have EVCs with weak or gentle peaks.

The observed strength and separation of the peaks in the $\ell - V$ diagram suggests that the Galactic bar must have an ILR. The central mass concentration, represented

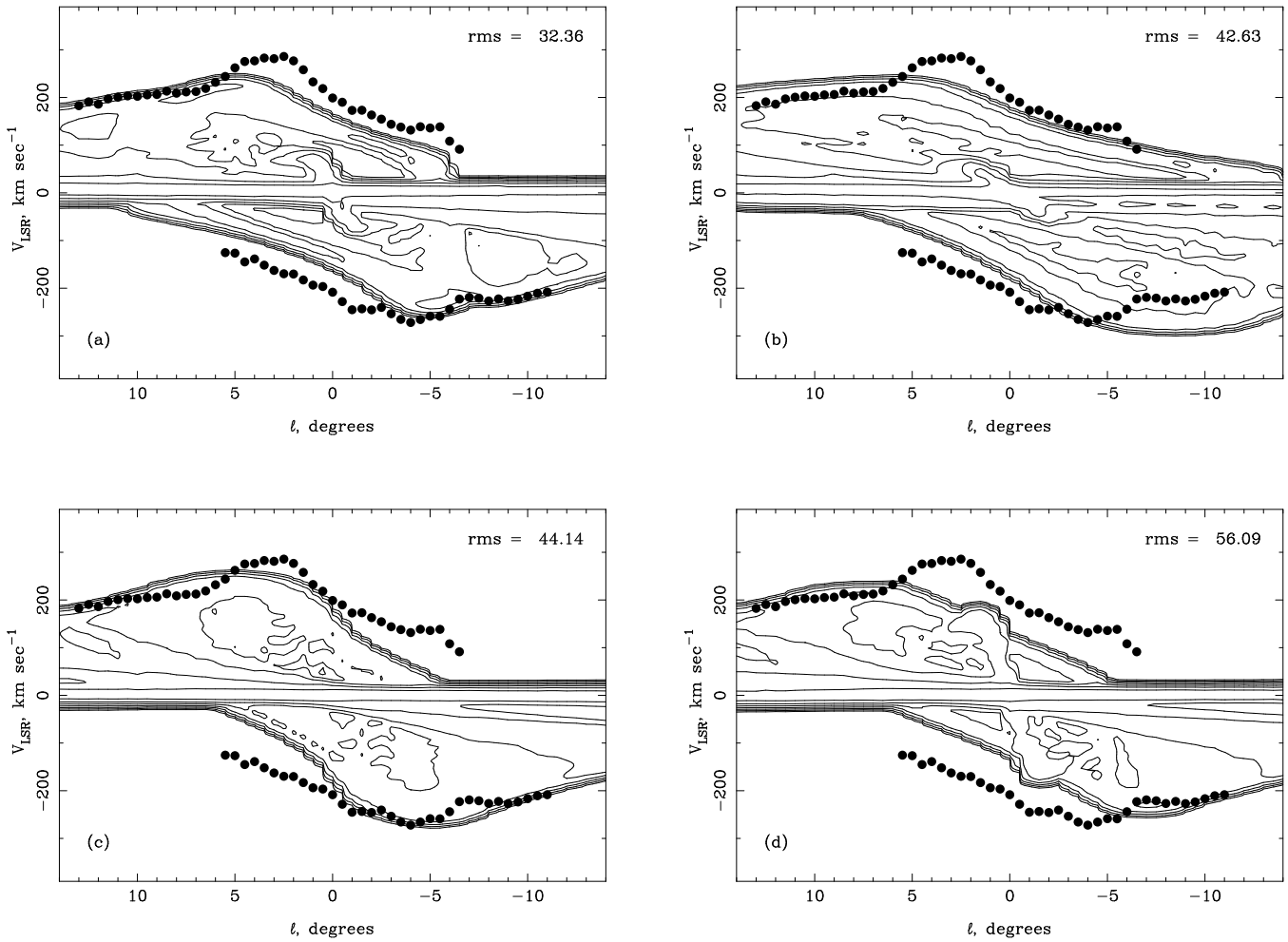

FIG. 13.— Longitude-velocity diagrams for several models with bars that have lower axis ratios than Model 1. The lowest contour is 1.7 $M_\odot\,kpc^{-2}\,deg^{-1}\,/\,km\ s^{-1}$ of total gas and the contours increase geometrically by a factor of 4. These models have EVCs whose peaks are not as sharp or as high as those observed.
(a) Model 29, $a = 3.6$ kpc, $b = 1.2$ kpc, $a/b = 3.0$, viewing angle 27°.
(b) Model 37, $a = 4.0$ kpc, $b = 1.3$ kpc, $a/b = 3.1$, viewing angle 55°.
(c) Model 39, $a = 2.5$ kpc, $b = 1.0$ kpc, $a/b = 2.5$, viewing angle 35°.
(d) Model 46, $a = 3.0$ kpc, $b = 1.3$ kpc, $a/b = 2.3$, viewing angle 32°.

in our model by the "bulge" component, is responsible for the ILR, and is also necessary to cause the sharply rising peaks in the EVC.

Our adopted modified Hubble profile for the central mass component has a uniform density core, whereas the luminosity density in the Milky Way rises all the way to the center as the ~ -1.8 power of the radius (Becklin & Neugebauer 1968). The finite resolution of the grid code vitiates attempts to simulate the effects of a central cusp; strong gradients in the angular velocity on scales below a few grid cells cannot be accurately represented. However, the small core radius in our best model, $r_c = 0.2$ kpc (four simulation grid cells), is well inside the ILR feature at $R \sim 0.4$ kpc. The existence of the ILR implied by the EVC peaks requires only a concentrated mass within that radius, so our conclusion is little affected by the details of the density profile.

7. DISCUSSION

We have shown that gas flow in a barred model of the Galaxy can fit many of the observed features of the H I $\ell - V$ diagram, most notably the emission in the forbidden quadrants and the sharp peaks in velocity. Our best fit model was arrived at through adjusting the free parameters by trial and error. Although the model has been tuned, the number of parameters is relatively small for a model of the Galactic potential. Furthermore, the complexity of the dynamics governing the gas response to the potential makes constructing a reasonably good model a non-trivial pursuit. This model does show that it is possible, and that the reservations of Jenkins & Binney (1994) regarding the ability of simple gas-dynamical models to reproduce the data are perhaps too pessimistic.

Our preferred model has a bar semi-major axis of 3.6 kpc. The bar component itself has an axis ratio of 4:1, although the "bulge" in our model should also be considered as part of the bar, and the axis ratio of the bar+bulge is somewhat fatter, approximately 3:1. The bar in this model rotates quickly, with a Lagrange radius of 5.0 kpc (bar pattern speed 42 km s^{-1} kpc^{-1}) and the bar major axis is inclined at 34° to our line of sight.

Our model 1 differs in a number of important respects

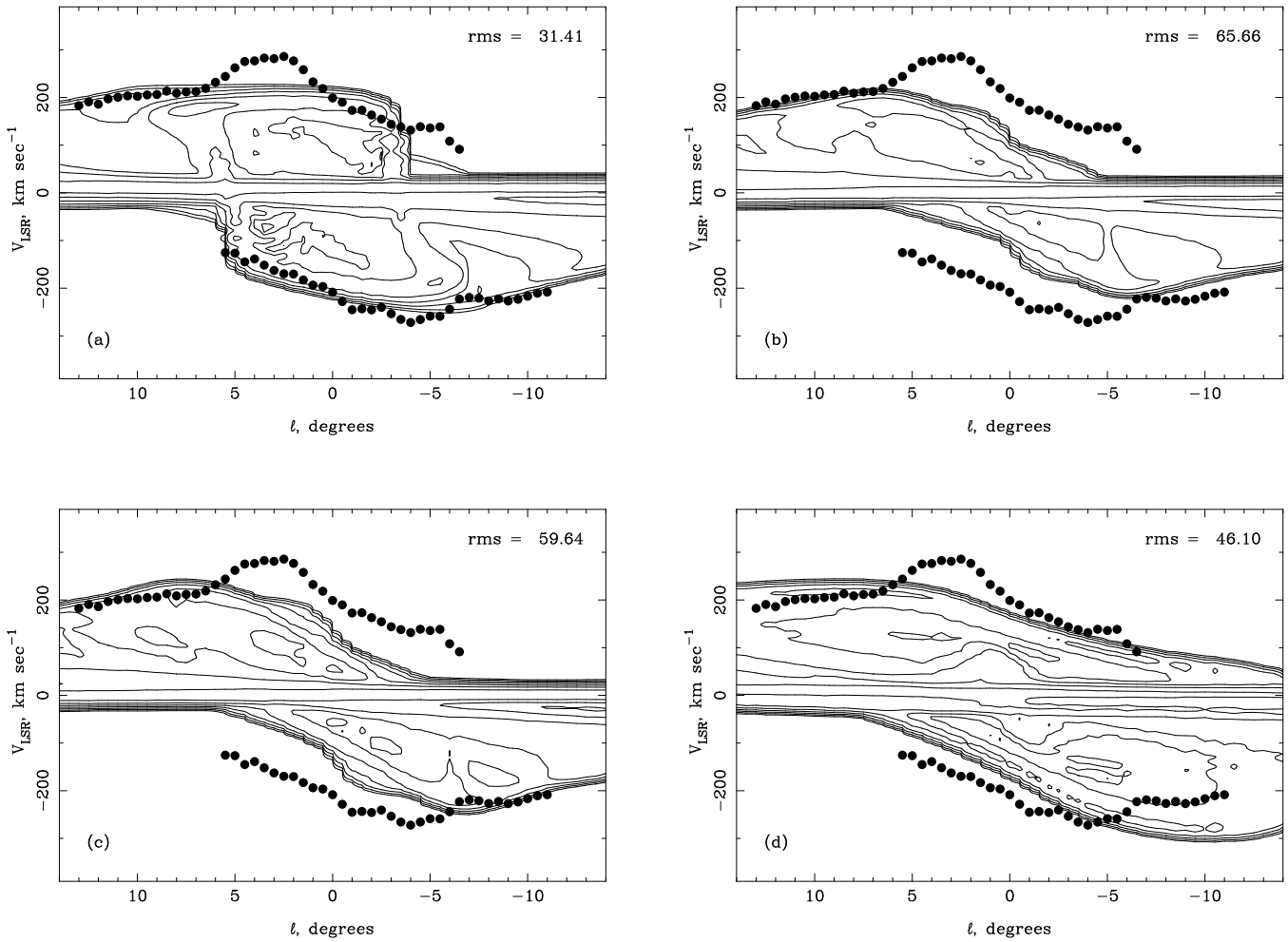

FIG. 14.— Longitude-velocity diagrams for several models which are less centrally concentrated than Model 1. The lowest contour is 1.7 $M_\odot\,kpc^{-2}\,deg^{-1}\,/\,km\ s^{-1}$ of total gas and the contours increase geometrically by a factor of 4. These models exhibit gently changing EVCs lacking the observed peaks.
(a) Model 27, $M_{bul}/M_{bar} = 0.019$, viewing angle 20°.
(b) Model 50, $M_{bul}/M_{bar} = 0.13$, viewing angle 20°.
(c) Model 48, $M_{bul}/M_{bar} = 0.16$, viewing angle 23°.
(d) Model 42, $M_{bul}/M_{bar} = 0.17$, viewing angle 55°.

from the models of the Milky Way bar proposed by Binney *et al.* (1991), and further developed by Jenkins & Binney (1994) and by Englmaier & Gerhard (1998). These authors favor a considerably smaller bar and a higher pattern speed, placing corotation at $R \sim 3.5$ kpc, because they employ a cusped x_1 orbit to give the narrow peaks at $\ell \simeq \pm 3°$. The x_2 orbit family, which is much less extensive in their models than in ours, gives a smaller peak very close to $\ell = 0$. While their models were developed to interpret the CO $\ell - V$ diagram, they fail to account for the large and extensive forbidden velocities seen in H I.

The strength and size of the bar are required by forbidden velocities in excess of 100 km s^{-1} extending as far as $\ell = \pm 6°$. Were the true viewing angle much less than our preferred 34°, as favored in some studies, the bar would have to be considerably longer to produce the observed forbidden velocities. Our constraint on viewing angle is not independent of the bar pattern speed, however, since slower bars give better fits when viewed at smaller angles. Models with a Lagrange radius of $R_L = 4.0$ to 6.0 kpc (bar pattern speed $\Omega_p = 54$ to 35 km s^{-1} kpc^{-1}), i.e. fast-rotating bars, are favored; models with higher R_L (lower Ω_p) have shock patterns in the gas that differ drastically from those observed in other barred galaxies. It is unlikely that the viewing angle could be forced below 25° to the bar major axis.

We interpret the narrow velocity peaks at $\ell \simeq \pm 3°$ as the signature of gas streaming along the bar past a nuclear ring in the Milky Way which lies close to the location of the inner Lindblad resonance. If the bar is strong, the high speed of these streams does not require an unusual radial mass profile – the flow patterns shown in Figures 2 & 4 arise from two mass distributions that both, when azimuthally averaged, give the circular velocity curve shown in Figure 3. The mass distribution in the inner Galaxy does have to be sufficiently concentrated for an ILR to be present, however; if this were not the case, the peaks would lie much closer to $\ell = 0$.

The location of the peaks at $\ell \simeq \pm 3°$ requires the semi-major axis of the nuclear ring to be ~ 400 pc – on the small end of the distribution of nuclear rings seen in other barred galaxies (Buta & Crocker 1993). As nuclear rings

in external galaxies are generally highly gas rich (Helfer & Blitz 1995; Sofue 1996; Rubin, Kenney & Young 1997), it is no surprise that the associated velocity peaks in the Milky Way stand out in CO as well as H I.

We note that the rotation curve of our preferred model, shown in Figure 3, indicates that the bulge and bar components together dominate the rotation curve in the inner few kpc of the Galaxy. We cannot isolate the contribution of the dark halo component, since our analytical model lumps the dark halo and the axisymmetric part of the disk together. However, since the Galaxy *does* have a disk, it is clear that the dark halo cannot be very dominant in this model. Although this potential is not a unique model of the Galaxy, as discussed above in Section 5, we believe that any model that fits the $\ell - V$ diagram will have to have non-axisymmetric motions as strong as those in Model 1 and, hence, a bulge+bar which dominates the rotation curve in the inner part of the Galaxy. Englmaier & Gerhard (1998) modeled the gas flow in the inner Galaxy, using models derived from COBE photometry. They found that the luminous matter must dominate over dark matter inside the solar circle, in order to match the terminal velocity curve in the non-forbidden quadrants.

We do not claim that because our model 1 gives a reasonable fit, the mass distribution in the inner Galaxy must necessarily be very close to the analytic form we have assumed. The real mass distribution in the inner Galaxy is undoubtedly more complex than our simple analytical model. A different form of mass distribution will yield somewhat different results for the best-fitting model parameters. However, we believe that the real mass distribution will resemble Model 1 in its chief details: the strength and size of the bar, presence of an ILR, and viewing angle which is not too close to end-on.

We have not attempted to satisfy the many other constraints on the shape of the inner Galaxy, such as COBE photometry, simultaneously. The model is broadly consistent with some results, such as the bar viewing angle determined by the IRAS point sources (Weinberg 1992), the magnitude offset of red clump stars (Stanek *et al.* 1997), and the distribution of OH/IR stars (Sevenster *et al.*1999). Fux (1999) has compared the appearance of arm features produced in a self-consistent model with features in the CO and H I $\ell - V$ diagrams; his preferred model has a bar of similar length, with an ILR, and which rotates quickly, but the preferred viewing angle is somewhat smaller, 25°, and the bar is fatter. Fux's comparison of models to data emphasizes high-density gas, while ours probes mostly low-density gas, which may be responsible for some of the differences. The viewing angles in Fux's best model and in ours are both incompatible with models which invoke a fairly end-on bar to account for the high microlensing optical depth towards the Galactic Bulge (Zhao & Mao 1996; see also Fux 1997).

The $\ell - V$ diagrams synthesized from fluid models are sensitive to the details of the potential and the viewing angle, and the comparison with the data is unaffected by extinction. For these reasons we believe that the technique has great power to discriminate among candidate models of the inner Milky Way. We may eventually hope to identify a model of the Galactic bar that satisfies photometric constraints and fits both the CO and H I kinematic data.

We are grateful to Dick van Albada and Lia Athanassoula for providing us with the gas dynamics code and for helpful comments and advice on its use, to Harvey Liszt for providing the data of Liszt & Burton (1980) in electronic form, and to an anonymous referee for a thoughtful report. This work was supported by NSF grant AST 96/17088 and NASA LTSA grant NAG 5-6037. BJW acknowledges support from a Carnegie postdoctoral fellowship.

REFERENCES

Athanassoula, E. 1992a, MNRAS, 259, 328
Athanassoula, E. 1992b, MNRAS, 259, 345
Bahcall, J. N., & Soneira, R. M. 1980, ApJS, 44, 73
Ball, J., Stark, A. A., Wilson, R. W., & Henkel, C. 1988, ApJ, 324, 223
Becklin, E.E., & Neugebauer, G. 1968, ApJ, 151, 145
Binney, J. J., Gerhard, O. E., Stark, A. A., Bally, J., & Uchida, K. I. 1991, MNRAS, 252, 210
Binney, J., Gerhard, O., & Spergel, D. 1997, MNRAS 288, 365
Binney, J., & Tremaine, S. 1987, Galactic Dynamics (Princeton: Princeton UP)
Blitz, L., Binney, J., Lo, K. Y., Bally, J., & Ho, P. T. P. 1993, Nature 361, 417
Blitz, L., & Spergel, D. N. 1991, ApJ, 379, 631
Bloemen, J.B.G.M., *et al.* 1986, A&A, 154, 25
Bronfman, L., Cohen, R. S., Alvarez, H., May, J., & Thaddeus, P. 1988, ApJ, 324, 248
Burton, W.B. & Liszt, H.S. 1978, ApJ, 225, 815
Burton, W.B. & Liszt, H.S. 1983, A&AS 52, 63
Burton, W.B. & Liszt, H.S. 1993, A & A, 274, 765
Buta, R., & Crocker, D. A. 1993, AJ, 105, 1344
Combes, F. 1996, in Barred Galaxies, IAU Colloquium 157, eds. R. Buta, D.A. Crocker, & B.G. Elmegreen (San Francisco: Astr. Soc. of the Pacific), 286
Dame, T., Ungerechts, H., Cohen, R. S., De Geus, E. J., Grenier, I. A., May, J., Murphy, D. C., Nyman, L.-A., & Thaddeus, P. 1987, ApJ, 322, 706
de Vaucouleurs, G. 1964, in The Galaxy and the Magellanic Clouds, IAU Symp. 20, eds. F. J. Kerr & A. W. Rodgers, (Canberra: Austr. Acad. Sci), 195
Dehnen, W. 1998, AJ 115, 2384
Dwek, E., Arendt, R. G., Hauser, M. G., Kelsall, T., Lisse, C. M., Moseley, S. H., Silverberg, R. F., Sodroski, T. J., & Weiland, J. L. 1995, ApJ, 445, 716
England, M.N. 1989, ApJ, 337, 191.
Englmaier, P., & Gerhard, O. 1997, MNRAS, 287, 57
Englmaier, P., & Gerhard, O. 1998, MNRAS (submitted)
Fux, R. 1997, A&A 327, 983
Fux, R. 1999, preprint astro-ph/9903154
Gerhard, O.E., & Vietri, M. 1986, MNRAS, 223, 377.
Gunn, J. E., Knapp, G. R., & Tremaine, S. D. 1979, AJ, 84, 1181
Helfer, T. T. & Blitz, L. 1995, ApJ, 450, 90
Hunter, J. H., Ball, J. R., & Gottesman, S. T. 1984, MNRAS, 208, 1
Kalnajs, A. 1992, in Dynamics of Disc Galaxies, ed. B. Sundelius (Göteborg: Göteborg Univ.), 323
Kent, S. M. 1992, ApJ, 387, 181
Kerr, F. J. 1967, in Radio Astronomy and the Galactic System, IAU Symp. 31, ed. H. van Woerden (London: Academic Press), 269
Kuijken, K. 1996, in Barred Galaxies, IAU Colloquium 157, eds. R. Buta, D.A. Crocker, & B.G. Elmegreen (San Francisco: Astr. Soc. of the Pacific), 504
Kuijken, K., & Tremaine, S. 1992, in Dynamics of Disc Galaxies, ed. B. Sundelius (Göteborg: Göteborg Univ.), 71
Jackson, P. D., & Kellmann, S. A. 1974, ApJ, 190, 53
Jenkins, A., & Binney, J. 1994, MNRAS, 270, 703
Kerr, F.J., & Westerhout, G. 1965, in Stars and Stellar Systems, v. 5, Galactic Structure, eds. A. Blaauw & M. Schmidt (Chicago: Chicago UP), 167
Lindblad, P. O., Hjelm, M., Högbom, J., Jörsäter, S., Lindblad, P. A. B., & Santos-Lleo, M. 1996, A&AS, 120, 403
Liszt, H. S. 1992, in The Center, Bulge, and Disk of the Milky Way, ed. L. Blitz (Dordrecht: Kluwer)
Liszt, H. S., & Burton, W. B. 1980, ApJ, 236, 779
Merrifield, M. R., & Kuijken, K. 1995, MNRAS, 274, 933.

Mihalas, D., & Binney, J. 1981, Galactic Astronomy, (New York: Freeman)
Moore, E. M., & Gottesman, S. T. 1995, ApJ, 447, 159
Mulder, W. A., & Liem, B. T. 1986, A&A, 157, 148
Nikolaev, S., & Weinberg, M.D. 1997, ApJ 487, 885
Oort, J. H. 1977, ARA&A, 15, 295
Ostriker, J. P., & Caldwell, J. A. R., 1983, in Kinematics, Dynamics and Structure of the Milky Way, ed. W.L.H. Shuter (Dordrecht: Reidel), 249
Pence, W.D., & Blackman, C.P. 1984, MNRAS, 207, 9.
Peters, W. L., III. 1975, ApJ, 195, 617
Prendergast, K. H. 1983, in Internal Kinematics and Dynamics of Galaxies, IAU Symp. 100, ed. E. Athanassoula (Dordrecht: Reidel), 215
Regan, M.W., Vogel, S.N., & Teuben, P.J. 1997, ApJ, 482, L143
Rougoor, G.W., & Oort, J.H. 1960, Proc. Nat. Acad. Sci., 46, 1
Rubin, V. C., Kenney, J. D. P. & Young, J. S., 1997, AJ, 113, 1250
Saraber, M.J.M., & Shane, W.W. 1974, A&A 36, 365.
Schmidt, M. 1965, in Stars and Stellar Systems, v. 5, Galactic Structure, eds. A. Blaauw & M. Schmidt (Chicago: Chicago UP), 513
Scoville, N.Z., Solomon, P.M., & Jefferts, K.B. 1974, ApJ, 187, L63
Sevenster, M.N. 1995, in Barred Galaxies, IAU Colloquium 157, eds. R. Buta, D.A. Crocker, & B.G. Elmegreen. (San Francisco: ASP), 536
Sevenster, M.N., Saha, P., Valls-Gabaud, D., & Fux, R. 1999, preprint astro-ph/9903426
Sofue, Y. 1996, ApJ, 458, 120
Stanek, K. Z. 1995, ApJ, 441, L29
Stanek, K. Z., Udalski, A., Szymanski, M., Kaluzny, J., Kubiak, M., Mateo, M., & Krzeminski, W. 1997, ApJ, 477, 163
van Albada, G. D. 1985a, A&A, 142, 491
van Albada, G. D. 1985b, in The Milky Way Galaxy, IAU Symp. 106, eds. H. van Woerden *et al.* (Dordrecht: Kluwer), 547
van Albada, T.S., & Sanders, R.H. 1982, MNRAS, 201, 303
Weinberg, M. D. 1992, ApJ, 384, 81
Weinberg, M. D. 1994, ApJ, 420, 597
Weiner, B.J., Williams, T.B., van Gorkom, J.H., & Sellwood, J.A. 1999, in preparation
Whitelock, P., & Catchpole, R. 1992, in The Center, Bulge, and Disk of the Milky Way, ed. L. Blitz (Dordrecht: Kluwer), 103
Zang, T.A. 1976, PhD thesis, M.I.T.
Zhao, H.S., & Mao, S. 1996, MNRAS 283, 1197

Table 1
Parameters of Models – Ordered Best-fit to Worst-fit

Model No.	Bulge $\rho_{0,\rm bul}$, $M_\odot$ pc^{-3}	Bulge r_c, kpc	Disk Σ_0, $M_\odot$ pc^{-2}	Disk R_c, kpc	Bar $\rho_{0,\rm bar}$, $M_\odot$ pc^{-3}	Bar a, kpc	Bar b, kpc	Lagrange radius R_L, kpc	Best–fit viewing angle $\phi_{\rm LSR}$	RMS velocity deviation, km s^{-1}
1	40	0.2	571	3.5	2.0	3.6	0.9	5.0	34°	16.54
2	40	0.2	571	3.5	2.0	3.6	0.9	4.0	32°	17.30
3	30	0.2	571	3.5	2.0	3.6	0.9	4.5	33°	17.90
4	40	0.2	571	3.5	2.0	3.6	0.9	8.0	8°	19.68
5	40	0.2	571	3.5	2.0	3.6	0.9	6.0	20°	19.82
6	30	0.2	571	3.5	2.5	2.5	0.83	8.0	73°	20.47
7	40	0.2	543	3.5	3.44	3.0	0.8	3.5	36°	20.82
8	40	0.2	571	3.5	2.0	3.6	0.9	7.0	14°	20.90
9	50	0.15	570	3.5	2.75	3.0	0.75	8.0	85°	21.21
10	70	0.15	571	3.5	2.75	3.0	0.75	3.6	27°	21.27
11	40	0.2	571	3.5	2.75	3.0	0.75	3.6	35°	21.31
12	50	0.15	570	3.5	2.75	3.0	0.75	7.2	91°	21.72
13	30	0.2	571	3.5	2.75	3.0	0.75	5.0	19°	21.84
14	50	0.2	571	3.5	2.75	3.0	0.75	3.6	38°	22.48
15	60	0.15	571	3.5	2.0	3.6	0.9	5.0	20°	22.49
16	70	0.15	570	3.5	2.75	3.0	0.75	3.6	26°	22.55
17	60	0.15	570	3.5	2.75	3.0	0.75	3.6	30°	22.64
18	65	0.15	570	3.5	2.75	3.0	0.75	8.0	79°	22.73[a]
19	30	0.2	571	3.5	2.75	3.0	0.75	3.6	28°	23.27
20	80	0.15	570	3.5	2.75	3.0	0.75	3.6	25°	23.79
21	65	0.15	570	3.5	2.75	3.0	0.75	3.6	23°	25.60
22	30	0.2	571	3.5	2.5	2.5	0.83	5.0	14°	26.86[b]
23	50	0.15	571	3.5	2.75	3.0	0.75	3.6	21°	28.44
24	40	0.2	543	3.5	2.2	3.0	1.0	3.5	32°	28.96
25	50	0.2	571	3.5	2.0	3.6	0.9	5.0	23°	29.07
26	30	0.2	571	3.5	2.5	2.5	0.83	4.0	29°	29.18
27	5	0.15	570	3.5	2.75	3.8	1.0	4.4	20°	31.41
28	40	0.2	571	3.5	1.8	3.0	1.0	3.5	31°	32.23
29	60	0.15	571	3.5	1.4	3.6	1.2	4.2	27°	32.36
30	50	0.15	686	3.5	2.75	3.0	0.75	3.6	29°	33.21
31	40	0.2	571	3.5	2.5	2.5	0.83	3.0	31°	33.34
32	100	0.15	570	3.5	2.75	3.0	0.75	3.6	17°	36.29
33	30	0.2	571	3.5	2.5	2.5	0.83	3.0	31°	37.91
34	80	0.15	571	3.5	1.4	3.6	1.2	4.2	27°	38.45
35	40	0.15	571	3.5	1.4	3.6	1.2	4.2	23°	39.49
36	25	0.15	571	3.5	2.75	3.0	0.75	3.6	25°	41.94
37	50	0.2	700	2.0	2.0	4.0	1.3	5.0	55°	42.63
38	40	0.2	543	3.5	1.53	3.0	1.2	3.5	31°	43.97
39	40	0.2	571	3.5	2.5	2.5	1.0	3.0	35°	44.14
40	50	0.15	570	3.5	1.55	3.0	1.0	3.6	23°	44.20
41	130	0.15	570	3.5	2.75	3.0	0.75	3.6	23°	45.55
42	35	0.2	800	2.0	2.4	4.0	1.3	5.0	55°	46.10
43	40	0.2	750	2.0	2.2	3.0	1.2	3.5	36°	49.09
44	40	0.25	467	3.0	2.2	3.0	1.2	3.5	49°	50.31
45	35	0.2	800	2.0	2.4	4.0	1.6	5.0	57°	54.66
46	200	0.1	567	3.0	1.5	3.0	1.3	3.5	32°	56.09
47	65	0.15	570	3.5	1.08	3.0	1.2	3.6	28°	58.08
48	35	0.15	600	3.0	1.8	3.0	1.3	3.5	23°	59.64
49	50	0.15	570	3.5	1.08	3.0	1.2	3.6	24°	62.94[c]
50	25	0.15	567	3.0	1.5	3.0	1.3	3.5	20°	65.66
51	15	0.15	570	3.5	0.8	3.5	1.5	4.2	23°	86.97

[a]RMS velocity deviation = 19.90 km s^{-1} at $\phi_{\rm LSR}$= –9°

[b]RMS velocity deviation = 17.68 km s^{-1} at $\phi_{\rm LSR}$= 103°

[c]RMS velocity deviation = 54.24 km s^{-1} at $\phi_{\rm LSR}$= –30°